Thermal and Electrical Characterization of a Micro-Hotplate for Calorimetry

By

Radhika Baliga

B.S. Electrical Science and Engineering
Massachusetts Institute of Technology, 2003

Submitted to the Department of Electrical Engineering and Computer Science
in Partial Fulfillment of the Requirements for the Degree of

Master of Engineering in Electrical Engineering and Computer Science
At the
Massachusetts Institute of Technology

September 2004

© Copyright 2004 Radhika Baliga. All rights reserved

MASSACHUSETTS INSTITUTE OF TECHNOLOGY
JUL 18 2005
LIBRARIES

The author hereby grants to M.I.T. permission to reproduce and distribute publicly paper and electronic copies of this thesis and to grant others the right to do so.

Author_____
Department of Electrical Engineering and Computer Science
July 8, 2004

Certified by_____
Amy E. Duwel, Ph.D.
Charles Stark Draper Laboratory Thesis Advisor

Certified by_____
Professor Joel Voldman
M.I.T. Thesis Advisor

Accepted by_____
Arthur C. Smith
Chairman, Department Committee on Graduate Theses

BARKER

[This page intentionally left blank.]

Thermal and Electrical Characterization of a Micro-Hotplate for Calorimetry

By
Radhika Baliga

Submitted to the
Department of Electrical Engineering and Computer Science
On July 8, 2004,
In partial fulfillment of the requirements for the
Degree of Master of Engineering of Electrical Engineering and Computer Science

Abstract

This thesis characterizes a micro-hotplate designed at Draper Laboratory. This hotplate will be integrated into a calorimetry system that measures the heat released or absorbed by a reaction. An analytical thermal model is developed to quantify the heat transfer mechanisms between the hotplate and the environment. The analytical model is verified through experimental measurements conducted with the device operating in both ambient conditions and vacuum. In ambient conditions, the heat transfer is dominated by air conduction as predicted by the model. Air conduction can be reduced by operating the device in a medium with a lower thermal conductivity. The relatively short timescale over which the hotplate comes to thermal equilibrium with the environment limits the types of reactions that can be measured with the device. The performance of the hotplate can be improved by operating it in vacuum, by constructing it from a material with a lower emissivity, or by decreasing its surface area. The noise spectral density of the hotplate's resistive temperature sensor is characterized. The hotplate's ability to resolve temperature is limited by the flicker noise in the sensor.

Draper Thesis Advisor: Amy E. Duwel, Ph.D.
Title: MEMS Group Leader, Charles Stark Draper Laboratory

M.I.T. Faculty Thesis Advisor: Professor Joel Voldman
Title: Assistant Professor, M.I.T. Department of Electrical Engineering and Computer Science

[This page intentionally left blank.]

Acknowledgements

July 8, 2004

There are several people at Draper and MIT that I would like to acknowledge for guiding my thesis work. I would like to thank Professor Joel Voldman at MIT for reviewing my work and being my faculty thesis advisor. I appreciate your time and your thoughtful comments and suggestions. I would also like to thank Amy Duwel, my advisor at Draper, for offering me the opportunity to work with the MEMS Group. Amy is extremely generous with her time and always has lots of excellent ideas. Amy was especially instrumental in helping me complete my thesis work smoothly and I appreciate her commitment. I would like to recognize Mark Mescher and Joe Donis for their guidance in the thermal modeling. I would also like to thank Keith Baldwin, Joan Orvosh, Eric Hildebrant, Chris O'Brien, and Tom King for their help with the electrical characterization of the device. The engineers that I have worked with at Draper are extremely knowledgeable and resourceful and I have definitely enjoyed collaborating with them over the last four years.

I would also like to thank my friends and classmates for their encouragement throughout my time at MIT. A few special friends that I would like to recognize are Areej, Avinash, Caroline, Hiro, Julia, Kim, Linda H., Linda L., Mike, Nahdia, Nancy, and Peter.

I am grateful to my family for all their love, support, and blessings. While it has not always been easy, my parents have made countless sacrifices to provide me and my brother with the best lifestyle and education. I appreciate all their hard work, dedication, and commitment to our family. I would like to thank my older brother, Sudhir, for setting high standards for me and for motivating me to challenge myself. I would also like to thank my grandparents for all their kind thoughts, prayers, and blessings.

This thesis was prepared at the Charles Stark Draper Laboratory, Inc., under Internal Research and Development Project Number 13122.

Publication of this thesis does not constitute approval by Draper or the sponsoring agency of the findings or conclusions contained herein. It is published for the exchange and stimulation of ideas.

[This page intentionally left blank.]

Contents

List of Figures

List of Tables

Chapter 1:

Introduction

Draper Laboratory has developed a novel MEMS hotplate using a hybrid silicon-polyimide process [1]. This hotplate can be integrated into a calorimetry system. Potential applications for this calorimeter relate to drug design and discovery. This thesis will thermally and electrically characterize Draper Laboratory's current micro-hotplate design.

This chapter provides background information to describe the motivation behind the development of this micro-hotplate. This chapter also explains the basics principles of calorimetry and describes its applicability to biological research. The advantages of incorporating MEMS technology into calorimeter design will be discussed and Draper Laboratory's first generation MEMS hotplate will be introduced.

1.1 Introduction to Calorimetry

A calorimeter is a device that measures the amount of heat released or absorbed by a reaction or phase transition [2]. The amount of heat released or absorbed per quantity of reactant indicates the change in enthalpy caused by the reaction. Depending on its mode of operation, a calorimeter can characterize a reaction by enabling the measurement of other parameters in addition to the enthalpy. These parameters include

binding affinity, melting point, glass transition, specific heat, entropy, stoichiometry, and free energy.

Two common modes of calorimetry are differential scanning calorimetry (DSC) and isothermal titration calorimetry (ITC). DSC is the most frequently used form of calorimetry. In addition to measuring the enthalpy of a phase transition, DSC is typically used to determine melting points, glass transitions, and specific heats of different substances. DSC is often used to determine the purity of a material when its thermal properties are well known. DSC is also utilized to characterize newly created materials whose thermal properties are unknown. ITC is used to thermally characterize binding reactions. ITC measures the heat that is absorbed or released when two substances bind to form a complex. It is also used to characterize the binding affinity coefficient between two substances. ITC is primarily used to study proteins and their interactions with ligands, DNA, lipids, carbohydrates, and other proteins. Biological applications of calorimetry will be discussed in subsequent sections.

In typical large-scale calorimeter designs the heat of a reaction is measured differentially using twin devices. The device that contains the reactants is called the sample and the other device is called the reference. In DSC, reactants are placed in the cell of the sample device only, while the reference remains empty. The reference can remain empty, in the case of DSC, or it can contain buffer solution, as is the case with ITC. In either case, reactions occur only in the sample cell. Each cell has a heater and a temperature sensor. The heater is usually a resistive element that can be biased with a current or voltage to heat the device by a dissipative process known as Joule heating. The temperature sensor may be a thermistor, thermopile, or resistive temperature detector

(RTD). A temperature control circuit continuously senses the temperature of both cells and modulates the heat supplied to each cell to maintain a zero temperature differential between the cells. The heat of a reaction is then determined by measuring the difference in power supplied to the heaters of the sample and reference cells over time.

Specifics of the temperature control scheme vary based on the mode of operation. In DSC, for instance, the temperature control signal for the reference cell is a linear ramp, which is specified in degrees per unit time. In ITC, however, the temperature control signal is a constant set-point. In both DSC and ITC, the control circuit adjusts the heat input to the sample cell to maintain an isothermal condition between sample and reference.

The remainder of this section discusses ITC in more detail. In an ITC experiment, a fixed quantity of reactant A (usually a protein) is placed in the sample cell while doses of reactant B (usually a ligand) are incrementally introduced, or titrated, into the sample and reference cells during the course of the experiment. Initially, the temperature control circuit supplies a constant amount of power to the heater of reference cell to maintain its temperature at the set-point, T_{set}. The power supplied to the heater of the sample cell, called the feedback power, is continuously modulated to ensure that the sample and reference are isothermal. After a dose of reactant B is injected into the sample and reference cells, the occurrence of an exothermic binding reaction will transiently generate heat in the sample cell and cause the temperature of the sample to increase above T_{set}. The power supply to the sample heater is shut off to null the temperature difference between the two cells. A block diagram of a typical system is shown in Figure 1.1. The amount of heat generated by the binding can be measured by monitoring the difference in

power supplied to the heaters of the sample and reference cells as the binding reaction takes place.

Figure 1.1 is a block diagram that explains the temperature control scheme for a typical isothermal titration calorimeter. For the control circuit of the reference, a voltage proportional to the desired set-point temperature is compared to a voltage signal proportional to the current temperature of the reference cell. The error signal, which reflects the difference between T_{set}, the set-point temperature, and T_r, the sensed temperature, is fed into a proportional-integral (PI) controller. This PI controller modulates $V_{r,heater}$, the voltage across the reference cell's resistive heating element, such that power is only input to the reference heater when the sensed temperature is lower than the set-point. Applying a voltage across the heater resistor causes the resistor to dissipate power in the form of heat. This process of converting electrical energy into heat is known as Joule heating. In the control circuit for the sample device, the error signal reflects the difference between the temperatures of the sample and reference. This error signal is fed into a PI controller which adjusts the sample heater voltage to maintain a zero temperature differential between the sample and reference cells.

The heat released by the binding reaction is measured by tracking the difference in the amounts of power supplied to the sample and reference calorimeters over time. A plot of this differential power as a function of time will have a transient singularity, or "dip", that indicates when the heat was released by the reaction. The amount of energy evolved is determined by integrating the power over the time interval during which the singularity occurred. This is illustrated in Figure 1.2.

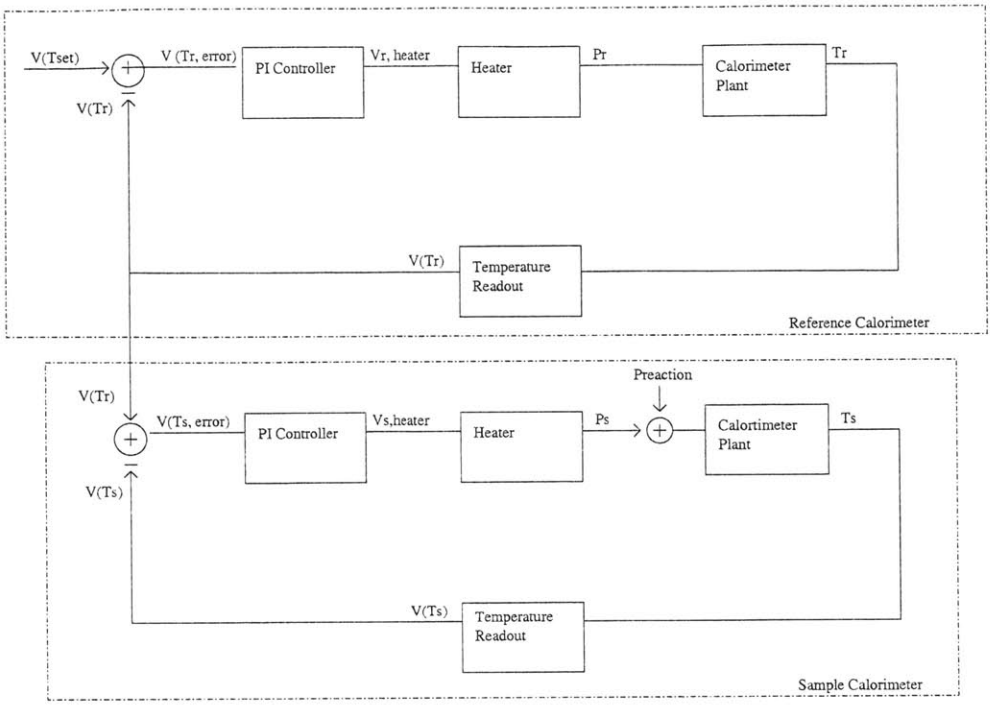

Figure 1.1. Block Diagram of a Typical Control Scheme for a Large-Scale Power Compensation Isothermal Titration Calorimeter. Subscripts r and s refer to the reference and the sample, respectively. V(*) denotes a voltage signal proportional to *.

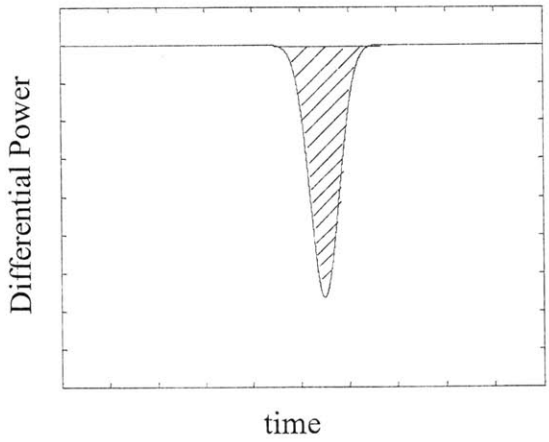

Figure 1.2. Measuring Heat Evolved Using Isothermal Titration Calorimeter. The curve is a plot of differential power as a function of time for a typical binding reaction. In this scenario, only one dose of reactant B is titrated into reactant A. The shaded area gives the amount of heat generated by the binding reaction.

Figure 1.2 shows the result of adding a single dose of reactant B to reactant A. In a complete titration experiment, reactant B is introduced incrementally, or titrated, into

reactant A multiple times, in equal and discrete amounts. This type of experiment measures the heat generation as a function of the amount of reactant B added to the cell. Figure 1.3 shows typical results obtained from a complete titration experiment. The top plot shows the differential heater power as a function of time. The area under each inverted peak is integrated to determine the heat released during each titration. The bottom plot shows the amount of heat released by the binding reactions as a function of the amount of B titrated into A. The asymptotic behavior results because there is only a finite amount of protein A in the sample cell. During the first few titrations, any amount of ligand B introduced to the sample cell is bound. As more ligand is introduced, saturation is eventually reached because there are fewer free molecules of A, and hence, fewer available bonding sites.

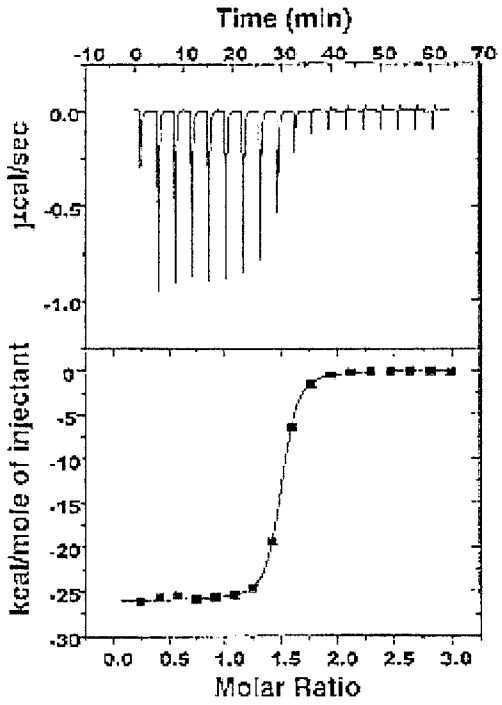

Figure 1.3. Typical Results from Isothermal Titration Calorimetry Experiment. The top plot shows the differential heater power as a function of time. The bottom plot shows the amount of heat released by binding reactions as a function of the amount of B in the sample cell. From [3].

1.2 Biocalorimetry

Biology is one field that makes extensive use of calorimetry. It has, therefore, motivated improvements in calorimeter design. The task of thermally characterizing interactions between proteins and other nanostructures is extremely challenging due to the small amounts of energy that are exchanged. Typical binding reactions of interest release approximately 10 kcal/mole of ligand [4]. In a typical ITC experiment, when solutions with micromolar concentrations of ligand are titrated into a protein solution in microliter quantities, the energy released per titration is on the order of ten microjoules. These sensitivity requirements have driven the development of microcalorimeters. Microcalorimeters are devices that can resolve the heat absorbed or released by a reaction down to at least one microjoule. One particular field of biology research that will benefit substantially from further advances in microcalorimetry is drug design. Measurements generated by differential scanning calorimetry (DSC) and isothermal titration calorimetry (ITC) characterize the strength and stability of the binding between drugs and their target proteins. In this way, DSC and ITC are tools that enable the effectiveness of prospective drugs to be evaluated.

DSC measures the onset of denaturation of a drug-protein complex and the change in enthalpy, ΔH, associated with the denaturation. This information indicates the stability of the binding between a drug and the target protein. When a drug binds to a target protein, it stabilizes the protein, causing the denaturation temperature, T_n, of the drug-protein complex to be higher than the denaturation temperature of the protein alone. Hence, as the calorimeter scans the temperature of the drug-protein solution, the shift in denaturation point can be identified. If two drugs can potentially bind to the same target

proteins at the same site, the substance that forms a complex with a higher denaturation point is a more stable complex [5].

While DSC characterizes binding by engineering the breakage of bonds, ITC evaluates the binding strength as bonds are formed. In an isothermal titration calorimetery experiment, heat is generated or absorbed when and if the drug binds to the target protein. ITC enables the measurement of the binding affinity coefficient, K_a; the number of binding sites n; enthalpy, ΔH; and entropy, ΔS [6]. A high binding affinity coefficient indicates a strong bond between a drug and its target protein.

1.3 MEMS Calorimetry

Recent developments in calorimetry have been motivated by increased interest in the study of nanostructures for use in biological, chemical, and engineering applications. MEMS has been identified as an approach for designing highly sensitive calorimeters that can be applied to a wide range of research areas from microfabrication processing techniques to biological systems.

This section reviews prior research in MEMS calorimetry by describing different calorimeter designs and their target applications.

Gerber, et al. present a bimetallic cantilever fabricated from aluminum (Al) and silicon nitride (Si_3N_4). When thermal energy impinges on the surface of the cantilever, the cantilever bends because of the mismatch in the thermal coefficients of expansion for the Al and Si_3N_4. The deflection of the cantilever tip is proportional to the amount of energy impinging on the cantilever's surface. The bending is determined optically by measuring the angle at which a light beam reflects off the surface of the cantilever. The system has a one millisecond response time and can measure heat fluxes on the order of

1nW, corresponding to a detection limit of 1 picoJoule [7]. Gerber, et al. propose that this micromachined cantilever may be used to study energy changes in single biological cells [8].

Allen, et al. were the first to demonstrate a thin-film MEMS-based differential scanning calorimeter with a sensitivity of 0.2nJ. This calorimeter has been used to compare the thermodynamic behavior of thin-film nanostructures with bulk materials for applications in solid-state microelectronics [9].

Allen's calorimeter uses a 1800Å silicon nitride membrane to hold the sample. The bottom surface of the membrane has a single resistive 1800Å nickel (Ni) thin-film stripe that heats the device and detects its temperature [9]. The device has an average heating rate of 32,000 °C/s and a cooling rate of approximately 2000 °C/s, indicating that the system is quasiadiabatic. Allen reports that 94% of the electric energy input is consumed by the calorimeter[9].

The device operates by simultaneously heating the sample and reference devices using pulses of current. The voltage across and the current through the sample and reference Ni thin-film resistors are monitored in real-time to determine melting point, heat capacity, and enthalpy changes. The calorimeter has been used to analyze properties of tin (Sn) thin-films. It has demonstrated a 120°C depression in the melting point of Sn as the thickness of the Sn sample is reduced from 20Å to 1Å. The device has a sensitivity of 1 nanogram for Sn [9].

1.4 MEMS and Biocalorimetry

The reported sensitivities of existing MEMS calorimeters suggest that MEMS can also be incorporated into the design of calorimetry systems that characterize drug-protein

interactions. There are numerous reasons for applying MEMS to biocalorimetry. Commercial microcalorimeters based on conventional designs perform studies on one reaction at a time. Consequently, the testing and screening of potential drugs using conventional ITCs becomes very lengthy and costly. The reduction in thermal mass in MEMS microcalorimeter designs reduces the time required to perform a single characterization. MEMS microcalorimeters can increase throughput even further because arrays of devices can be easily fabricated and used to perform many tests simultaneously. This increases the number of target proteins that can be studied for one particular drug. Furthermore, MEMS microcalorimeters reduce the amount of sample required to perform a reliable measurement. Whereas a microcalorimeter based on traditional ITC design may require 1μg of drug, a MEMS microcalorimeter would require only 50 picograms to 1 nanogram of material. Hence, MEMS microcalorimetery is an attractive option because it reduces the amount of drug required by a factor of 1000 over standard techniques and facilitates the screening of prospective drugs which are rarely in abundance.

1.5 Draper Microcalorimeter Design

Draper Laboratory's calorimeter is a novel MEMS device fabricated using a hybrid silicon-polyimide process. The calorimeter is square polyimide hotplate connected to a silicon frame by four polyimide tethers. Analytes in solution are dispensed on the top surface of the polyimide membrane. Interdigitated serpentine-like platinum resistors for heating and temperature sensing are fabricated on the bottom surface of the hotplate. Control electronics are placed off-chip, allowing the calorimeter to operate in different modes, including isothermal titration or differential scanning modes. The ultimate goal is to use this calorimeter for applications in drug design and screening.

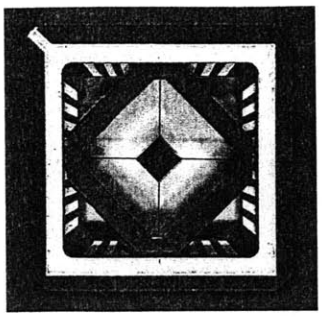

Figure 1.4. Draper Laboratory's MEMS Microcalorimeter Hotplate. The device is mounted in a 36-pin leadless ceramic chip carrier.

1.6 Thesis Outline

In this thesis Draper Laboratory's first generation of microcalorimeter hotplates will be thermally and electrically characterized through analytical models and experimental measurements. Chapter 2 elaborates on Draper's hotplate design and provides an overview of the fabrication process. Chapter 3 presents thermal models to quantify heat transfer mechanisms using both lumped-element thermal circuit analysis and finite element modeling. These thermal models were originally developed by Mark Mescher at Draper. This thesis contributes a more in-depth analysis and provides a framework for device optimization. Chapters 4 and 5 describe the experiments designed to empirically determine the thermal model parameters. Results from these experiments are discussed and compared to the theoretical thermal models developed. Chapter 6 characterizes the noise in the calorimeter sensor to determine the fundamental limitations on the calorimeter's ability to measure temperature. The electronics and experimental approaches in Chapters 4 through 6 were designed by Draper. This thesis contributes data collection, data analysis, and final sensitivity analysis. The results of the thermal and electrical characterization lead to a discussion of how the Draper microcalorimeter hotplate can be improved in future design iterations.

Chapter 2:

Draper Calorimeter Design

This chapter elaborates upon the design of Draper Laboratory's first generation of microcalorimeter hotplates that were introduced in Chapter 1.

2.1 Device Structure and Geometries

Five different device geometries of the Draper microcalorimeter have been fabricated. The geometries are summarized in Table 2.1. Pictures of a device are shown in Figure 2.1. Each device from the first four geometries listed in Table 2.1 is comprised of a 1875 μm x 1.875 μm x 5 μm suspended polyimide plate that is connected to, and thermally isolated from, a silicon frame by four polyimide tethers. These devices vary in the dimensions of the tethers as described in Table 2.1. Devices of the fifth geometry each have a complete polyimide membrane that extends to the edges of the silicon frame. These full membrane devices are designed for mechanical robustness.

Table 2.1. Device Geometries.

Tether Length (μm)	Polyimide Tether Width (μm)
2790	35
2790	95
1403	95
2790	300
Full membrane device, no polyimide tethers	Full membrane device, no polyimide tethers

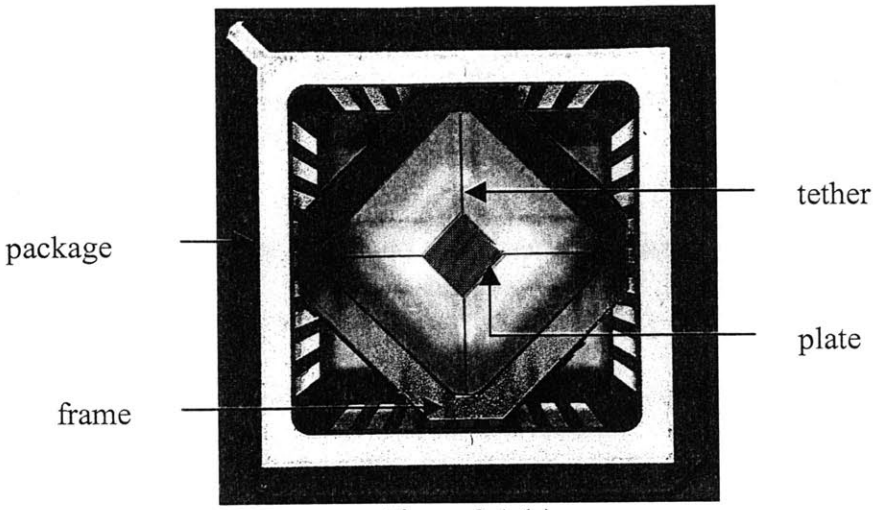

Figure 2.1 (a)

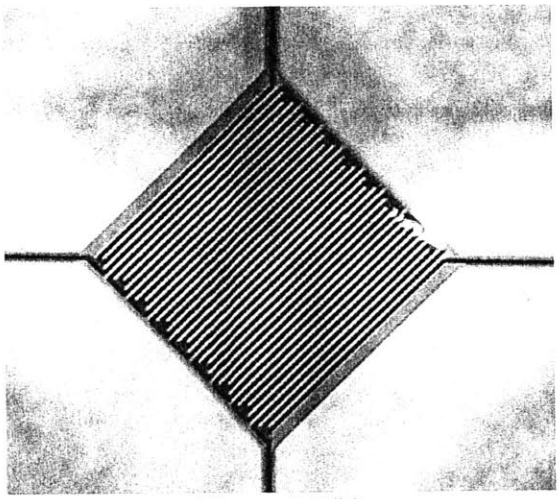

Figure 2.1(b)

Figure 2.1. Pictures of a Draper Microcalorimeter. Figure 2.1(a) shows a calorimeter device mounted in a 36 pin LCCC package. Figure 2.1(b) is a close-up view of the plate and resistive heater and sensor.

Two interdigitated serpentine-like resistors are fabricated on the bottom surface of the polyimide plate. One resistor is used for heating the plate and the other is used for sensing the temperature of the plate. Both resistors have a nominal resistance on the order of one kilohm. The serpentine resistor design was implemented for several reasons. First, it enables the resistors to be evenly distributed over the surface area of the plate. Second, the distribution of the sensor allows the resistance of the sensor to reflect the

average value of the temperature across the entire surface of the plate. Furthermore, the serpentine-like traces also provide a way to maximize the electrical resistances of the heater and sensor.

The Draper calorimeter was intended to operate in vacuum, at room temperature. Under these conditions, the dimensions of the tethers were designed to achieve thermal time constants between 15 seconds and 30 seconds. This time constant indicates the time required for the device to reach thermal equilibrium with the environment. The dimensions of the plate were selected to minimize the thermal mass of the system. The dimensions of the plate were also designed to easily accommodate samples that will be dispensed in nanoliter quantities by a Microdot robot.

2.2 Materials

This section explains the rationale used to chose the materials from which to fabricate the device.

2.2.1 Polyimide Plate and Tethers

Several factors were considered when selecting a material to form the thermal plate. Polyimide was chosen because it is a thermally stable polymer that can withstand a range of temperatures. The decomposition temperature of polyimides is approximately 500°C. This is advantageous when operating the calorimeter in differential scanning mode because the calorimeter must be heated over a wide temperature range to measure denaturation temperatures. Polyimide is also beneficial because of its chemical stability and biocompatibility. These are important factors because the device will be used to characterize interactions between several biological and chemical agents.

The same material was used to form the plate and the tethers to simplify the fabrication of the device. Polyimide is ideal from a fabrication standpoint because it is easy to deposit and pattern. Polyimides have low thermal conductivities that can range from $0.12\frac{W}{m \cdot K}$ to $0.20\frac{W}{m \cdot K}$. The low thermal conductivity makes polyimide an ideal material for the tether design. The tethers are constructed to have a low conductance to minimize power losses from the device to the ambient. Ideally, the plate should be constructed to have a high conductance. This ensures that the temperature of the plate is uniform through its thickness. The plate thickness must be minimized to increase the conductance through the thickness of the plate. Both the plate and the tethers have the same thickness. Minimizing the thickness of the polyimide layer also decreases the cross-sectional area of the tethers, thereby decreasing the conductance through the length of the tethers.

2.2.2 Platinum Resistors

Platinum has become the industry standard for resistive temperature detectors (RTDs) because of its outstanding properties, which include linearity and stability. These same properties were considered when selecting platinum as the material for the resistive temperature sensor.

The calorimeter design utilizes platinum as a resistive temperature detector because there is a linear relationship between the temperature and resistance of platinum over a broad temperature range. For industry standard platinum RTDs, the relationship between resistance and temperature is given by the Callendar-Van Dusen equation shown in (1) and (2) [10].

$$R(T) = R_0(1 + AT + BT^2 + C(T^4 - 100T^3)) \quad \text{for -200°C <T<0°C} \quad (1)$$

$$R(T) = R_0(1 + AT + BT^2) \quad \text{for 0°C <T<850°C} \quad (2)$$

where R(T) is the resistance (in Ohms) of the RTD at temperature T (in °C)
R_0 is the resistance (in Ohms) of the RTD at 0°C
A = 3.90830e-3
B = -5.77500e-7
C = -4.18301e-12

While the Callendar-Van Dusen equation is inherently non-linear, we may neglect the higher order terms by setting B and C equal to 0 and use a simple linear approximation to express the resistance temperature relationship without introducing significant error. Figure 2 compares the Callendar-Van Dusen equation to the first-order linear approximation described above.

For the Draper calorimeter, the relationship between the sensor resistance and temperature is approximated as a linear curve and is expressed as shown in (3) and (4).

$$R_{sensor} = R_0(1 + \alpha\Delta T) \quad (3)$$

$$\Delta T = T_{sensor} - T_{amb} \quad (4)$$

where R_{sensor} is the sensor resistance in Ohms at temperature T_{sensor}
R_0 is the sensor resistance in Ohms at $T = T_{amb}$, or at $\Delta T = 0$
α is the temperature coefficient of resistance (TCR) in $°C^{-1}$
T_{sensor} is the temperature of the sensor in °C
T_{amb} is the ambient temperature in °C

Linearity between sensor resistance and temperature is a design consideration because it simplifies the design of control electronics for a closed-loop temperature controller.

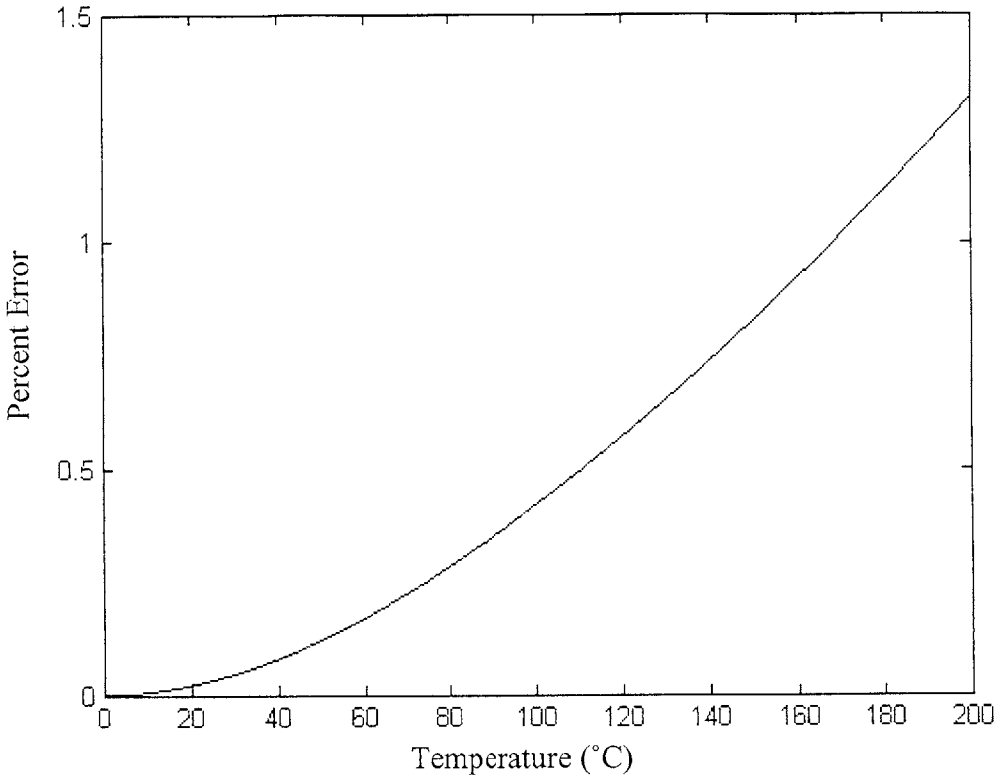

Figure 2.2. Comparison of the Callendar-Van Dusen Equation and its First Order Linear Approximation. The plot reflects the percent error between the exact Callendar-Van Dusen equation and the linear first-order approximation to the Callendar-Van Dusen equation over a range of temperatures spanning from 0°C to 200°C.

The sensor is fabricated from platinum because it is an inert metal that does not oxidize. Platinum exhibits superior performance in terms of long-term stability and repeatability because it does not experience significant electrical degradation over time.

The heater performs its function by Joule heating, a process by which electrical current passing through a resistive element converts electrical energy into thermal energy. The heater resistor is also fabricated from platinum to simplify to the fabrication process flow.

2.3 Fabrication

This section gives a brief overview of the fabrication process for the Draper microcalorimeter. Schematics of the device are shown at each step of the process in Figure 3. The fabrication process for the calorimeter is compatible with existing processes.

1. Grow 1.0μm thermal oxide on 550μm thick silicon (Si) wafer.
2. Spin, bake, and pattern 5.0 μm layer of polyimide on top of the 1.0μm thermal oxide.
3. Spin and bake negative photoresist. Expose and develop regions that will not have platinum traces. Deposit 300Å layer of titanium (Ti) to promote adhesion of the platinum (Pt). Then deposit a 1100Å layer of Pt to form the resistive heater and sensor. Lift-off titanium, platinum, and resist, leaving behind the desired interdigitated sensor and heater resistors.
4. Sputter, pattern, and wet etch gold (Au) to form four 0.5μm thick pad electrodes.
5. Attach a handle wafer with polyvinyl alcohol (PVA) and deposit resist on the backside of the first silicon wafer to pattern the frame for the device.
6. Plasma etch the silicon to form the frame. Etch the thermal oxide on the frontside to expose the polyimide.
7. Remove die from handle wafer.

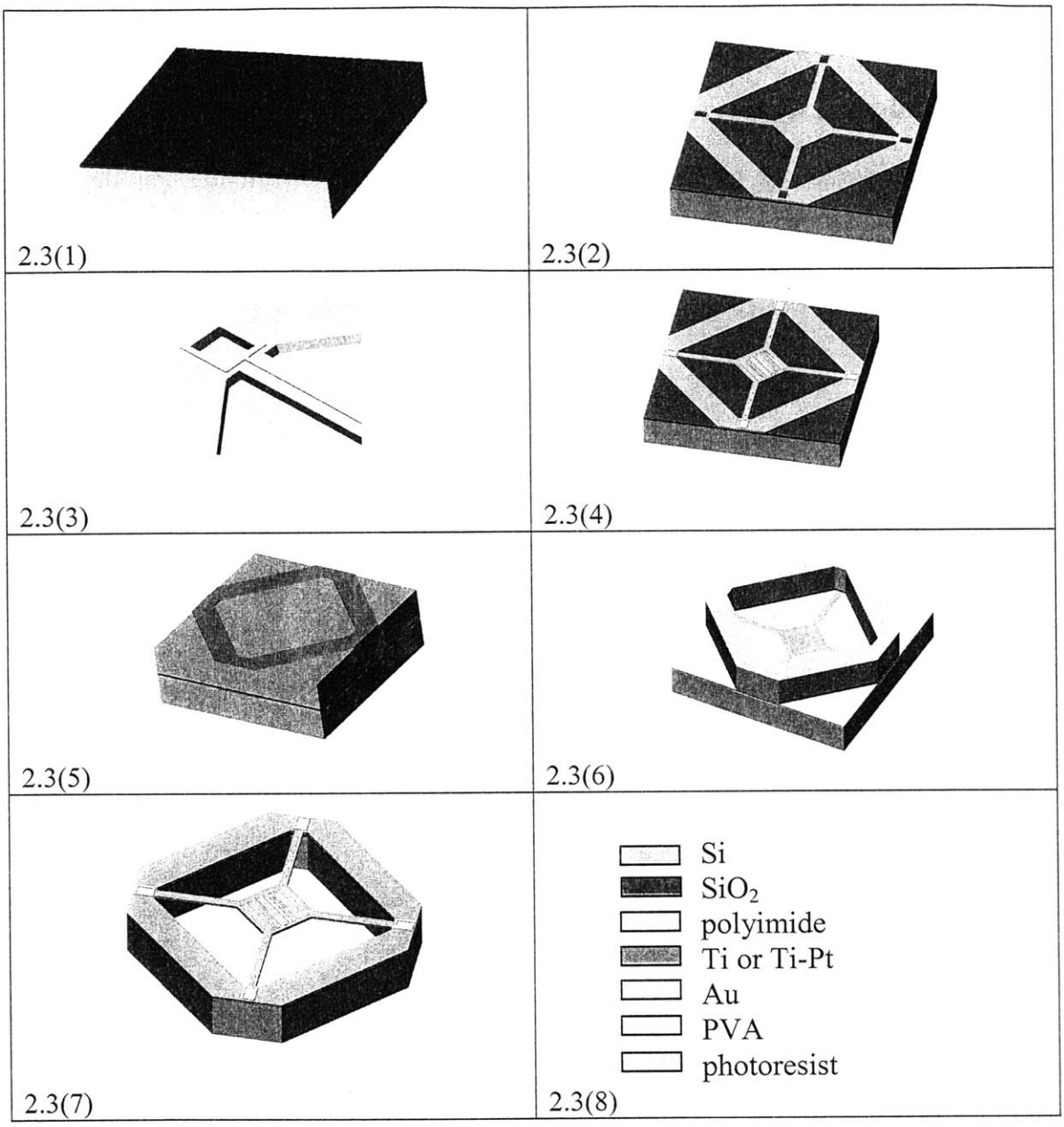

Figure 2.3. Schematics of Fabrication Process. Numbers enclosed in parentheses correspond to the fabrication steps listed above. Figure 2.3(8) identifies the materials used in the fabrication.

2.4 Packaging

Each die is packaged in a 36-pin leadless ceramic chip carrier (LCCC) using conductive epoxy to bond the sensor and heater electrodes to the pins of the LCCC. See Figure 2.1(a) for a picture of a packaged device.

2.5 Sample Handling Interface

Analytes in solution are dispensed on the top surface of the plate using a Biodot Robot. The Biodot can accurately dispense as little as 10nL of solution onto the plate. The devices are plasma treated before use to create a hydrophilic surface. Samples placed on a plasma treated membrane will wet the entire surface of the membrane.

Chapter 3:

Time Constant Analysis

This chapter discusses the time constants associated with a calorimetry system. We derive the time constants that are dictated purely by the design of the microcalorimeter device.

3.1 Overview of Relevant Time Constants

Several timescales must be considered when designing the calorimeter. Table 3.1 provides a description of the relevant time constants. Figure 3.1 shows the desired placement of these time constants.

Table 3.1. Description of Time Constants

Time Constant	Description
τ_{plate}	Timescale for equilibration of plate with reaction
$\tau_{measure}$	Measurement time associated with electronics
τ_{mixing}	Timescale for mixing of reactants
τ_{Rx}	Timescale of reaction
τ_e	Timescale for equilibration of plate with environment

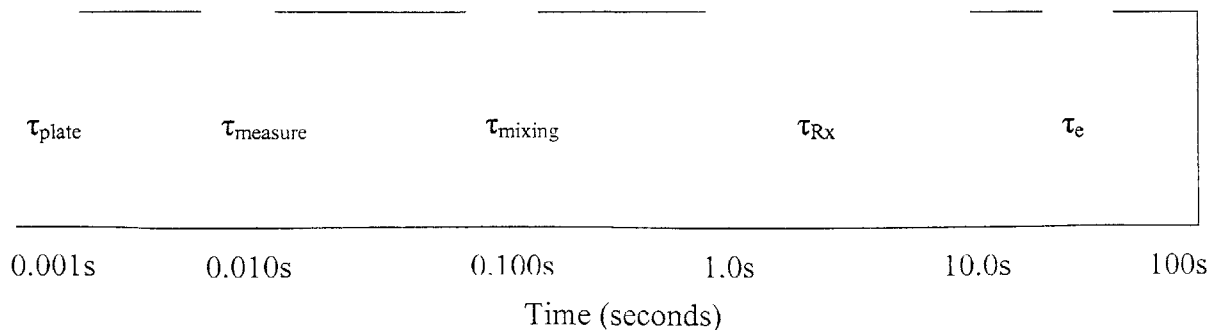

Figure 3.1. Relative Placement of Time Constants.

τ_{plate} is the characteristic time for the temperature distribution through the thickness of the plate to equilibrate with the reaction. The derivation of this time constant will be presented in this chapter. We will show that this time constant is governed by the plate dimensions and material properties, and can, therefore, be modified.

τ_{mixing} is the time required for the reactants to mix via mechanisms including diffusion and convection. This time constant will vary depending on the particular reaction of interest. It is a function of several variables including the size of the reactant molecules. The time constant of a reaction, τ_{Rx}, is also a characteristic that varies from reaction to reaction. We leave the investigation of parameters τ_{mixing} and τ_{Rx} for future work.

τ_e is the timescale for the plate to equilibrate with the environment. The heat released or absorbed by the reaction is measured with a set of electronics that has an associated measurement time, τ_m. Transient temperature changes caused by the reaction must be measured before the plate achieves thermal equilibrium with environment. Therefore, we require τ_m to be substantially smaller than τ_e. This chapter will derive τ_e for the current calorimeter design. τ_e is dependent on the level of thermal isolation between the calorimeter and its environment. The heat transfer mechanisms between the calorimeter and the environment include conductive losses through the tethers, conductive losses through the air, and radiative losses.

3.2 Equilibration Time of Calorimeter Plate with Reaction

The time constant through the plate thickness, τ_{plate}, indicates the amount of time necessary for the plate to reach thermal equilibrium with transient temperature changes caused by a reaction. Consider placing a sample on the plate that provides a constant

heat flux to the top surface of the plate. We assume that the edges of the plate are insulating and that heat is conducted only through the thickness of the plate, in the z direction. The plate thickness is denoted as h_{plate}.

The temperature distribution through the thickness of the plate as a function of time can be determined by the heat equation shown in (1). The temperature, U, is a function of z, t, and D. z is the position along the thickness, t is the time, and D is the diffusivity constant. The power input to the calorimeter plate will vary from reaction to reaction. Because the power input is arbitrary, the heat equation is solved subject to the idealized insulating boundary conditions shown in (2) to simplify the analytical calculation. FEMLAB, a finite element modeling tool, will be used to show that the time constant through the thickness of plate is insensitive to the boundary condition on the top surface of the plate.

$$\frac{\partial U}{\partial t} = D \cdot \frac{\partial^2 U}{\partial z^2} \tag{1}$$

$$\text{where } D = \frac{\kappa_{PI}}{c_{PI} \cdot \rho_{PI}}$$

$$\frac{\partial U}{\partial z}(0,t) = \frac{\partial U}{\partial z}\left(h_{plate}, t\right) = 0 \tag{2}$$

The method used to solve the equation is separation of variables [11]. U is expressed as the product of two functions; one function, Z(z), is only dependent on position and the other function, T(t), is dependent on time.

$$U(z,t) = Z(z) \cdot T(t) \tag{3}$$

Substituting (3) into (1) yields (4).

$$\frac{Z''}{Z} = \frac{T'}{DT} = -\lambda^2 \tag{4}$$

The left-hand side of (4) is used to determine U as a function of z.

$$Z''(z) + \lambda^2 Z(z) = 0 \tag{5}$$

The general solution to (5) is given in (6). Boundary conditions are used to determine all possible λ's that solve (5). These λ's are also known as the eigenmodes of the solution. For a non-trivial solution, (9) implies that λh_{plate} is an integer multiple of π.

$$Z(z) = A\cos(\lambda \cdot z) + B\sin(\lambda \cdot z) \tag{6}$$
$$Z'(z) = -A\lambda\sin(\lambda \cdot z) + B\lambda\cos(\lambda \cdot z) \tag{7}$$
$$Z'(z=0) = 0 \Rightarrow B = 0 \tag{8}$$
$$Z'(z = h_{plate}) = 0 \Rightarrow Z'(z) = -A\lambda\sin(\lambda \cdot h_{plate}) = 0 \Rightarrow \lambda h_{plate} = n\pi \tag{9}$$

where n is an integer

$$\lambda^2 = \frac{n^2\pi^2}{h_{plate}^2} \tag{10}$$

The temperature as a function of position is shown in (11)

$$Z_n(z) = \cos(\frac{n\pi z}{h_{plate}}) \tag{11}$$

From (4) we also obtain (12). This first-order linear differential equation with constant coefficients can be used to find the time constant as shown in (13). The expression for temperature as a function of time is shown in (14).

$$T'(t) + D\lambda^2 T(t) = 0 \tag{12}$$
$$\tau = \frac{1}{\lambda^2 D} = \frac{h_{plate}^2 c_{PI}\rho_{PI}}{n^2\pi^2\kappa_{PI}} \tag{13}$$
$$T_n(t) = \exp(-\frac{n^2\pi^2 Dt}{h_{plate}^2}) \tag{14}$$

Finally, the temperature is expressed as a function of both space and time is presented in (15). Because the heat equation is linear, the total solution can be expressed as a linear combination of all solutions that satisfy (1) and (2).

$$U(z,t) = U_0 + \sum_{n=1}^{\infty} U_n \cos(\frac{n\pi z}{h_{plate}}) \exp(-\frac{t}{\tau_n}) \tag{15}$$

Following (15), we see that the time response is dominated by the lowest order eigenmodes. For n=1, the time constant is calculated in (16). The time constant in (16) is the timescale for the plate to equilibrate with sample.

$$\tau_{plate} = \tau_{n=1} = \frac{1}{\omega_{n=1}} = \frac{(5\mu m)^2 \cdot 1088 \frac{J}{kg \cdot K} \cdot 1390 \frac{kg}{m^3}}{\pi^2 \cdot 0.126 \frac{W}{m \cdot K}} = 3.04e-5 \sec \tag{16}$$

A finite element model is developed using FEMLAB to verify the plate time constant. It is a two-dimensional heat conduction model that uses the geometry and material properties of the calorimeter plate to determine the temperature distribution through the thickness of the plate. First, the model is solved using eigenvalue analysis, subject to the insulating boundary conditions shown in (2). The lowest eigenvalue that generates a temperature distribution that varies through the thickness of the plate is 3.3e4 rad/sec. This corresponds to a 30 μsec time constant. The time constant derived through FEMLAB agrees with the time constant that was calculated in (16). The results of the simulation are shown in Figure 3.2.

Next, we modify the boundary condition to provide a constant heat flux to the top surface of the plate. We use an unreasonably large heat flux of 2.8e5 $W \cdot m^{-2}$. This corresponds to 1 Watt of power distributed over the area of the plate. The results of this FEMLAB simulation shown in Figure 3.3 illustrate that there is no change in the time

constant through the plate thickness. Changing the boundary condition from a uniform heat flux to an insulating boundary condition does not generate any significant changes in the time constant for heat transfer through the plate thickness.

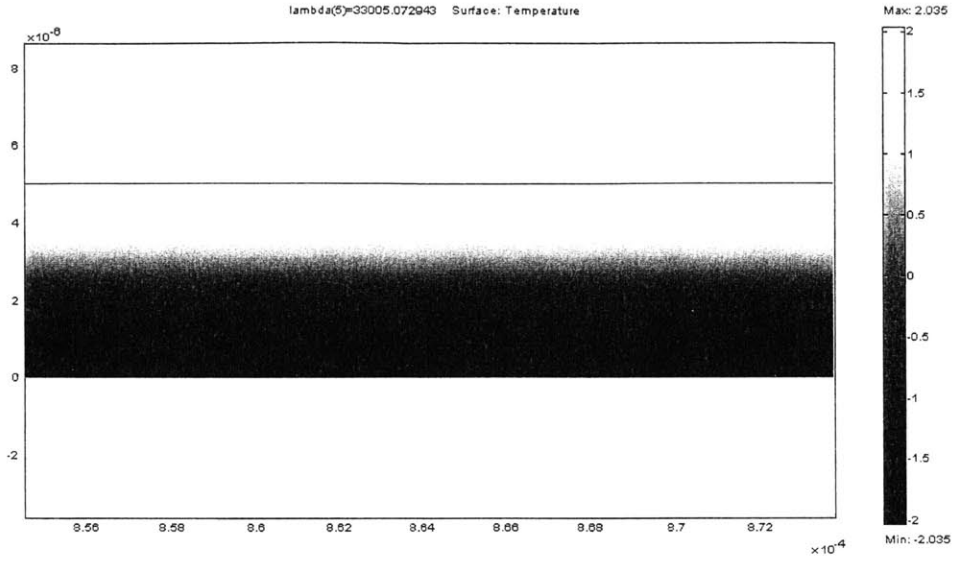

Figure 3.2. Temperature Distribution through Thickness of Plate for ω=3.3e4 rad/sec when Insulating Boundary Conditions are Applied.

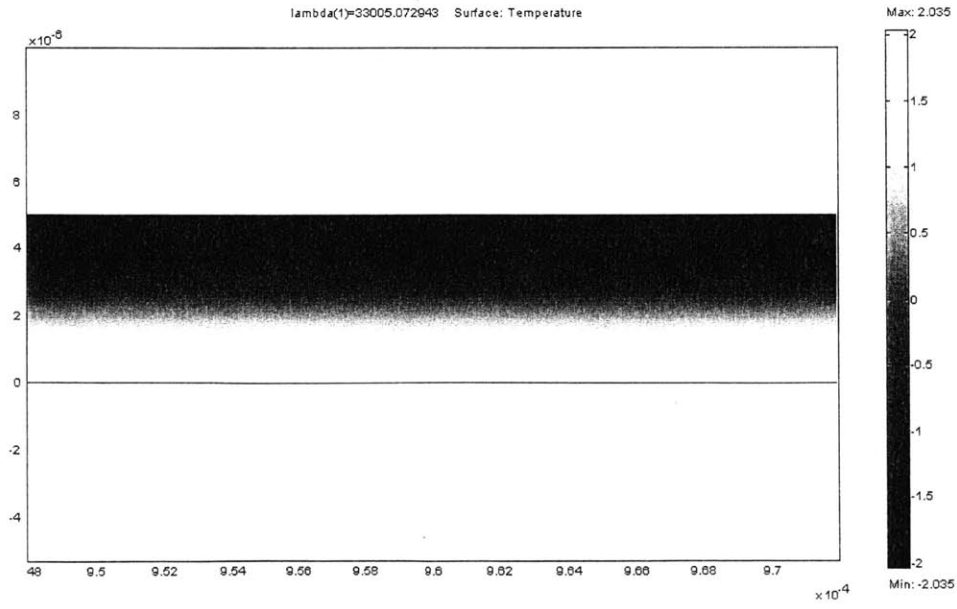

Figure 3.3 Temperature Distribution through Thickness of Plate for ω=3.3e4 rad/sec when a Uniform Heat Flux of 2.8e5 $W \cdot m^{-2}$ is Applied to Top Surface of Plate. This heat flux corresponds to 1 Watt of power distributed over the area of the plate.

3.3 Equilibration Time of Calorimeter Plate with Environment

In this section, we estimate τ_e, the time for the calorimeter plate to equilibrate with the environment. τ_e is estimated through an analytical thermal model that describes the heat transfer mechanisms between the calorimeter and environment. The calculations in this section were guided by Mark Mescher and Joe Donis at Draper Laboratory. The thermal model is presented as a lumped element thermal circuit, analogous to an electrical circuit. In thermal circuits, currents model heat flow, voltages model temperature, resistors model resistance to heat flow, and capacitors model thermal mass.

The analytical lumped element model for the calorimeter plate and tethers will be a first-order RC circuit, as shown in Figure 3.4. The current source models power input to the device. The lumped thermal resistance, R_t, models the heat transfer via conduction, convection, and radiation. The thermal capacitor, C_t, models the thermal mass of the calorimeter plate and reactants.

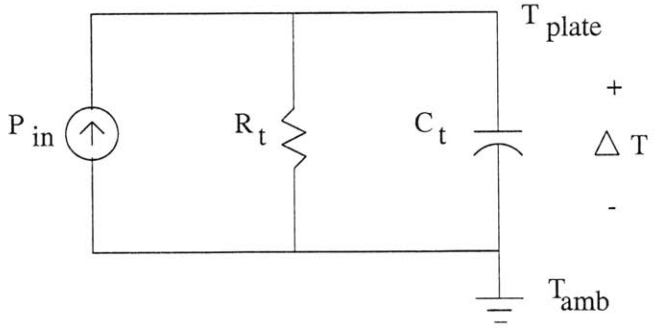

Figure 3.4. First-order Thermal Circuit to Model Heat Transfer Mechanisms between Calorimeter and Environment.

Following the model in Figure 3.3, the time constant τ_e is the product of the lumped element thermal resistance and capacitance.

$$\tau_e = R_t C_t \tag{17}$$

We use the lumped-element circuit model to derive τ_e for different geometries of the Draper microcalorimeter. The derivation of τ_e is based on several assumptions. We assume that the temperature distribution of the polyimide plate is spatially uniform. The temperature of the plate will be denoted as T_{plate}. The silicon frame is assumed to be in thermal equilibrium with the ambient temperature, T_{amb}. The calculations presented here assume that the calorimeter operates in still, dry air at atmospheric pressure. The ambient temperature is assumed to be 298K.

3.3.1 Lumped Element Thermal Resistance

In determining the lumped element thermal resistance, heat transfer via conduction, convection, and radiation are considered. This section explains how conduction, convection, and radiation can be modeled using thermal circuits. We compute the lumped element thermal resistance of the calorimeter geometry with four tethers of length 2790μm and width 95μm in the body of the text in detail. Lumped element thermal resistances for the other geometries with tethers are shown in Table 3.2.

3.3.1.1 Conduction

When neighboring molecules in a medium collide, energy is transferred from highly energetic molecules to less energetic molecules. Because these highly energetic molecules are associated with higher temperatures, heat is conducted from warmer regions to cooler regions. Conductive heat transfer is governed by Fourier's Law of Heat Conduction. Fourier's Law for one-dimensional heat conduction through a medium is shown in (18). It states that heat flux is proportional to the negative of the spatial temperature gradient.

$$q = -\kappa \frac{dT}{dx} \tag{18}$$

where q is heat flux, or heat flow per unit area normal, in [W/m^2],
κ is the thermal conductivity of the medium in [W/(m·K)],
$\frac{dT}{dx}$ is the spatial temperature gradient [K/m],

Consider a rectangular wall of material with thermal conductivity κ, cross-sectional area A, thickness L, and heat flow $\dot{Q}$ which is normal to area A. One face of the wall is at temperature T_1 and the opposite face is at temperature T_2 as shown in Figure 3.5. The wall can be broken into differential volumes with area A and thickness Δx. Under the assumption that no heat is generated in the differential volume, the heat flowing into the volume at x is identical to the heat flow out of the volume at $x+\Delta x$. Hence, the heat flow through the slab is continuous and constant as shown in (19).

$$\dot{Q}|_x = \dot{Q}|_{x+\Delta x} = \dot{Q} \tag{19}$$

Noting that the heat flow is the product of the heat flux and the area of the wall, Fourier's Law of Heat Conduction is used to obtain (20).

$$\dot{Q} = qA = -\kappa \frac{dT}{dx} A \tag{20}$$

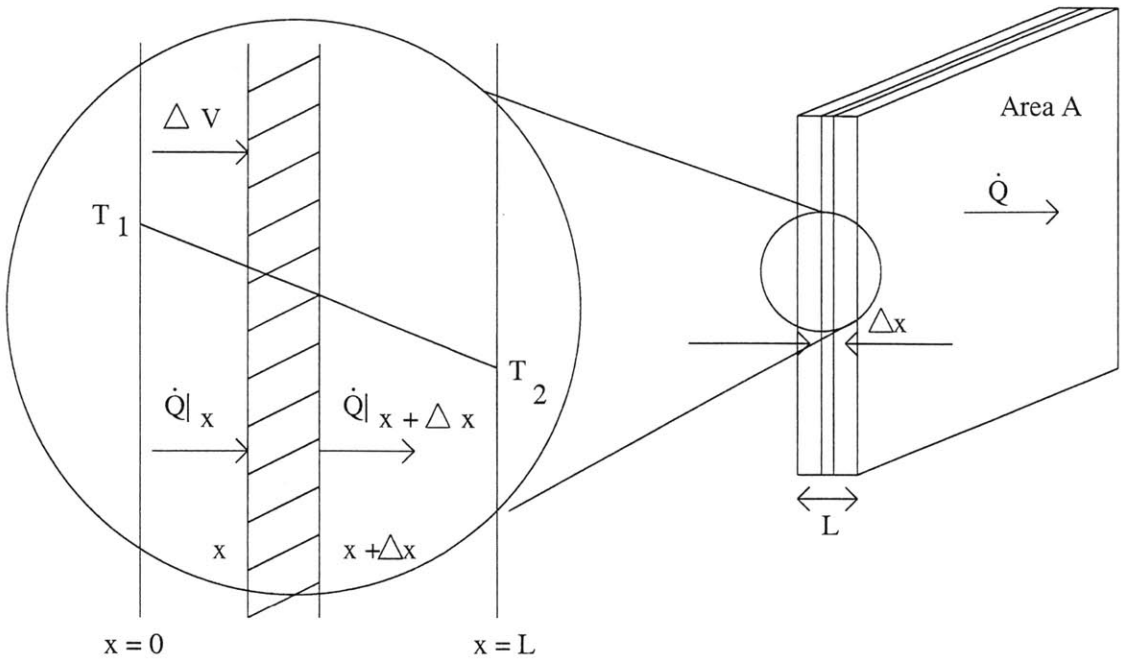

Figure 3.5. One-dimensional Conduction Through a Wall. Taken after [12].

Separating variables and integrating across the entire thickness of the wall, yields (21) and (22).

$$\frac{\dot{Q}}{A}\int_0^L dx = -\kappa\int_{T1}^{T2} dT \tag{21}$$

$$\frac{\dot{Q}}{A}L = \kappa(T_1 - T_2) \tag{22}$$

Rearranging (22) yields (23).

$$\dot{Q} = \frac{\kappa A}{L}(T_1 - T_2) \tag{23}$$

Equation (23) closely resembles Ohm's law from the electrical domain. In an electrical circuit, a resistor, R, relates the amount of current, I, that can flow through a potential difference, V, as illustrated by Ohm's Law in (24).

$$I = \frac{1}{R} \cdot V \tag{24}$$

where I is current
R is resistance
V is voltage

In the thermal domain, $\dot{Q}$ is analogous to current and the temperature difference T_1-T_2 is analogous to a potential difference. Thermal resistances define the heat flow through a temperature difference. The thermal resistance due to conduction is given by (25).

$$R_{t,cond} = \frac{L}{\kappa A} \tag{25}$$

3.3.1.1.1 Conduction through Tethers

Consider conductive heat transfer through the four tethers that connect the polyimide plate to the silicon frame. One end of each tether is at temperature T_{plate}, while the opposite end, connected to the silicon frame, is at temperature T_{amb}. Each tether is a three-layer structure. The top layer is 5 μm of polyimide, the middle layer is 0.13μm of titanium, and the bottom layer is 0.20μm of platinum. For a single tether, the thermal resistance due to conduction is the parallel combination of the thermal resistance due to each layer. For a single tether, the contributions to the conductive thermal resistance by the polyimide (PI), titanium (Ti), and platinum (Pt) layers are shown in (26), (27), and (28), respectively.

$$R_{t,cond,tether,PI} = \frac{L_{tether}}{\kappa_{PI} A_{cs,PI}} = \frac{L_{tether}}{\kappa_{PI} t_{PI} w_{tether}} = \frac{2790\mu m}{0.126\frac{W}{m \cdot K} \cdot 5\mu m \cdot 95\mu m} = 4.7e7\frac{K}{W} \tag{26}$$

where L is length of the tether
κ is thermal conductivity
t is thickness
w is width

$$R_{t,cond,tether,Ti} = \frac{L_{tether}}{\kappa_{Ti} A_{cs,Ti}} = \frac{L_{tether}}{\kappa_{Ti} t_{Ti} w_{metal}} = \frac{2790\mu m}{21.0\frac{W}{m \cdot K} \cdot 0.13\mu m \cdot 35\mu m} = 2.9e7\frac{K}{W} \quad (27)$$

$$R_{t,cond,tether,Pt} = \frac{L_{tether}}{\kappa_{Pt} A_{cs,Pt}} = \frac{L_{tether}}{\kappa_{Pt} t_{Pt} w_{metal}} = \frac{2790\mu m}{71.6\frac{W}{m \cdot K}.0.20\mu m \cdot 35\mu m} = 5.6e6\frac{K}{W} \quad (28)$$

The polyimide tether length and width vary by geometry (see Chapter 2 section 1). The titanium and platinum metal trace widths are uniform for all geometries at 35μm. The thermal resistance due to conduction for a single tether is shown in (29).

$$R_{t,cond,tether} = \frac{1}{\sum_x \frac{1}{R_{t,cond,tether,x}}} = 4.3e6\frac{K}{W} \quad (29)$$

The thermal resistance due to conduction through all four tethers is the parallel combination of thermal resistances of four single tethers.

$$R_{t,cond,4tethers} = \frac{1}{4} \cdot R_{t,cond,tether} = 1.1e6\frac{K}{W} \quad (30)$$

3.3.1.1.2 Conduction through Air

We now compute the thermal resistance due to conduction through air. First consider the conduction through the air from the top surface of the polyimide plate. The air conducts heat from the surface of the plate to infinity. For a circular disk with radius r, the thermal resistance attributed to air conduction from the disk to a point at infinity is given by (31) [13].

$$R_{t,air,disk,\infty} = \frac{1}{4\kappa_{air} r} \quad (31)$$

where κ_{air} is the thermal conductivity of air
r is the radius of the disk

While the calorimeter plate is a square, (31) can still be applied by calculating an equivalent radius, denoted by r_{eff}, for the square geometry. r_{eff} is determined by equating the surface area of a disk with radius r_{eff} to the surface area of a square plate with length l_{plate}.

$$r_{eff} = \frac{l_{plate}}{\sqrt{\pi}} \tag{32}$$

The thermal resistance due to air conduction from a contact spot on a square plate to infinity is given in (33).

$$R_{t,air,topsurface,\infty} = \frac{1}{4\kappa_{air} r_{eff}} = \frac{\sqrt{\pi}}{4\kappa_{air} l_{plate}} = \frac{\sqrt{\pi}}{4 \cdot 0.0267 \frac{W}{m \cdot K} \cdot 1.875mm} = 8.85e3 \frac{K}{W} \tag{33}$$

We now consider air conduction from the bottom surface of the plate to the leadless ceramic chip carrier (LCCC) package. There is a 1 mm gap between the plate and the package. We estimate the thermal resistance to air using a parallel plate approximation as shown in (34).

$$R_{t,air,bottomsurface} = \frac{g}{\kappa_{air} A_{plate}} = \frac{1mm}{0.0267 \frac{W}{m \cdot K} \cdot (1.875mm)^2} = 1.1e4 \frac{K}{W} \tag{34}$$

where g is the gap between the plate and package
κ_{air} is the thermal conductivity of air
A_{plate} is the area of the plate

The thermal resistance from a contact spot on the plate to infinity should place an upper bound on the air conduction resistance. The result shown in (34) is counterintuitive. The air conduction resistance from a contact spot on the plate to infinity should be higher than the air conduction resistance from the bottom surface of the plate to the package. The model used in (34) to derive the air conduction resistance from the

bottom surface of the plate to the package assumes that the air conduction resistance increases linearly with the gap between the plate and package. As the size of the gap approaches the length of the plate, this simple model breaks down. The model is analogous to a parallel plate capacitor model. In the capacitor model, as the distance between the plates approaches the dimensions of the plates, the fringing fields must be taken into account. We provide a similar treatment here, following [14]. G_0 represents the increase in conductance due to these fringing fields on all four sides of the plate.

$$R_{t,air,bottomsurface} = \frac{1}{G_{t,air,bottomsurface}} \tag{35}$$

$$G_{t,air,bottomsurface} = \frac{\kappa_{air} A_{plate}}{g} + G_0 \tag{36}$$

$$G_0 = 4 \cdot 0.26 \cdot \kappa_{air} \cdot l_{plate} \tag{37}$$

$$R_{t,air,bottomsurface} = 6.9e3 \frac{K}{W} \tag{38}$$

Figure 3.6 shows the three models considered in finding the air conduction resistance. For this hotplate, the simple parallel plate model can be used when the gap is less than 0.2mm, or less than 11% the length of the plate. For larger gaps, the parallel plate model with the fringing fields approximation should be used. When the gap is larger than 1.6 mm, or at least 85% of the plate length, the approximation for air conduction from a contact spot to infinity should be used.

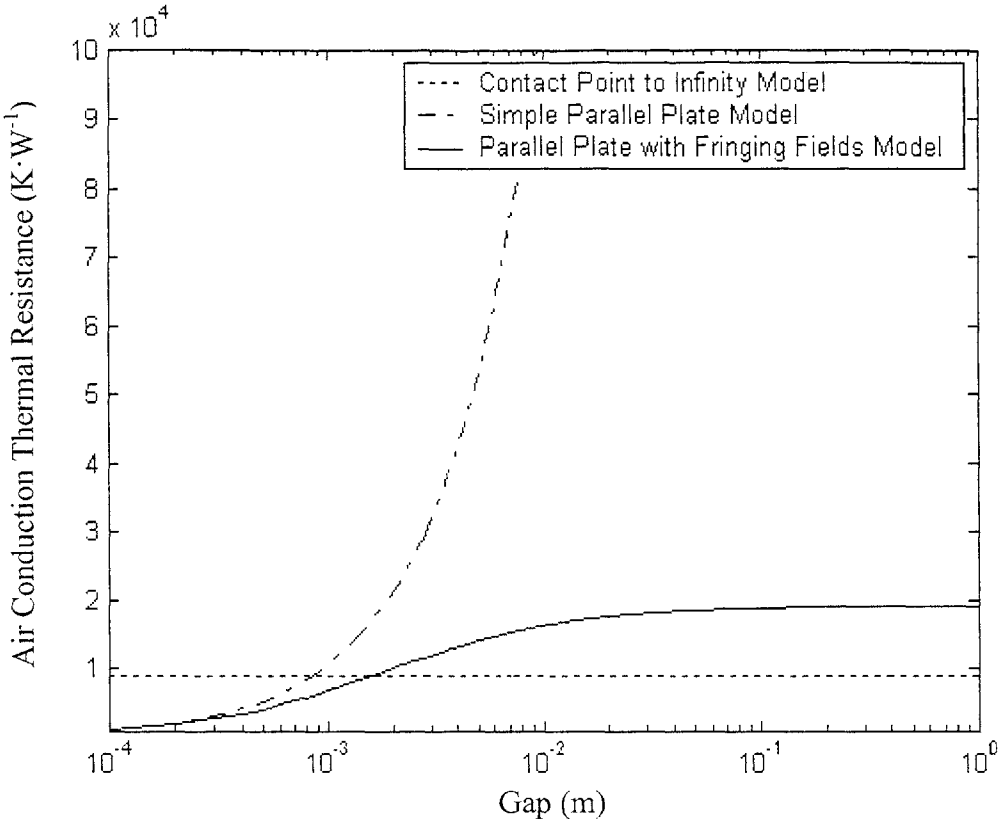

Figure 3.6. Air Conduction Thermal Resistance Determined using Three Different Models.

The total thermal resistance to air from the top and bottom surfaces of the plate can be expressed as shown in (39).

$$R_{t,cond,air} = \frac{1}{\frac{1}{R_{t,air,topsurface,\infty}} + \frac{1}{R_{t,air,bottomsurface}}} = 3.9e3\frac{K}{W} \tag{39}$$

3.3.1.2 Convection

Convection occurs when heat is transferred between a bounding surface and a moving fluid. Depending on the nature of the fluid flow, heat transfer via convection can be classified as forced convection or free convection. In forced convection, the flow is created by an external source, such as a fan or pump. In free convection, the flow is

caused by buoyant forces that are created by density differences that arise from temperature gradients within the fluid. Consider a hotplate sitting in still air. The air that comes into direct contact with the surface of the plate increases in temperature. This warmer air now ascends because it is less dense than the surrounding air. In this way, the buoyant forces create a vertical movement of air in which cooler air displaces warmer air. Regardless of the fluid flow regime, convective heat flow from the surface into the fluid is described by Newton's Law of cooling.

$$\dot{Q} = h_c A_s (T_s - T_f) \tag{40}$$

where h_c is the convective heat transfer coefficient
A_s is the exposed surface area
T_s is the temperature of the surface
T_f is the temperature of the fluid.

h_c depends on various factors including surface geometry, and properties of the fluid, such as thermal conductivity and velocity. The thermal resistance due to convection is given by (41).

$$R_{t,conv} = \frac{1}{h_c A_s} \tag{41}$$

In stagnant room air, convection can be neglected for plates of sufficiently small areas [15]. We will assume that heat transferred via convection from the calorimeter is negligible.

3.3.1.3 Radiation

Matter at a finite temperature emits energy in the form of thermal radiation. The amount of energy emitted depends on the temperature of the body. Radiative heat transfer deals with the exchange of thermal radiation between bodies. Irradiation, G

[W/m^2], is the term for flux of radiant energy incident on a body. Radiosity, J [W/m^2], is the flux of thermal energy leaving a body by emission or reflection.

For simplicity, we first consider blackbody radiation. A blackbody is a surface that absorbs all incident radiant energy and allows energy to leave solely through emission. The radiosity of a blackbody is given by the Stefan-Boltzmann law, shown in (42). The radiosity of a blackbody, which we denote here by J_{black}, is the blackbody emissive power.

$$J_{black} = \sigma_{SB} T^4 \tag{42}$$

where J_{black} is the radiosity of a blackbody
σ_{SB} is the Stefan-Boltzmann constant 5.67e-8 [$W/(m^2 \cdot K)$] ,
T is the temperature of the body in [K]

Consider placing a blackbody inside a black enclosure in which the ambient environment is at temperature T_2. When equilibrium is achieved, both the enclosure and blackbody will be at temperature T_2. There is no net radiant flux between isothermal bodies. The energy flux incident on the blackbody equals the energy flux leaving the body as shown in (43).

$$G_{black} = J_{black} = \sigma_{SB} T_2^4 \tag{43}$$

Suppose now that the temperature of the blackbody is increased to T_1, while the temperature inside the enclosure remains at T_2. The radiosity emitted by the blackbody is given in (44).

$$J_{black} = \sigma_{SB} T_1^4 \tag{44}$$

The net flux of energy leaving the surface of the blackbody is shown in (45).

$$q_{black} = J_{black} - G_{black} = \sigma_{SB} T_1^4 - \sigma_{SB} T_2^4 \tag{45}$$

The heat flow, $\dot{Q}$, between the blackbody and the ambient surroundings is obtained in (46).

$$\dot{Q} = q_{black} A = (J_{black} - G_{black}) A = \sigma_{SB} A(T_1^4 - T_2^4) \tag{46}$$

Blackbodies are ideal surfaces. Real surfaces absorb and emit less radiation than blackbodies. For a real surface, the rate at which thermal energy is absorbed per unit surface area is dependent on the absorptivity, α. The absorptivity varies from 0 to 1 and describes how efficiently a real surface absorbs thermal radiation with respect to a blackbody.

$$G_{real} = \alpha G_{black} = \alpha \sigma_{SB} T^4 \tag{43}$$

Similarly, the rate at which thermal energy is emitted by a real surface is dependent on the emissitivity, ε. The emissivity can vary between 0 and 1 and it describes how efficiently a real surface can emit energy with respect to a blackbody.

$$J_{real} = \varepsilon J_{black} = \varepsilon \sigma_{SB} T^4 \tag{47}$$

Gray surfaces are a class of real surfaces for which the emissivity and absorptivity are equal.

Consider the radiative heat transfer between two graybodies. Object 1 is at temperature T_1 and has emissivity ε_1 and object 2 is at temperature T_2 and has emissivity ε_2. The radiative heat flow is a function of temperatures T_1 and T_2, emissivities ε_1 and ε_2, and the geometries of object 1 and 2. The heat flow can be written as shown in (48).

$$\dot{Q}_{12} = \sigma_{SB} A_1 F_{12} (T_1^4 - T_2^4) \tag{48}$$

F_{12} is known as the transfer factor and it captures the dependence on emissivity and geometry. If surface 1 is enclosed inside surface 2, then the transfer factor can be approximated as ε_1. The heat flow can then be written as shown in (49).

$$\dot{Q}_{12} = \sigma_{SB} A_1 \varepsilon_1 (T_1^4 - T_2^4) \tag{49}$$

Equation (46) is linearized to express the heat flow in terms of the temperature difference, T_1-T_2.

$$\dot{Q}_{12} = \sigma_{SB} A_1 \varepsilon_1 (T_1^4 - T_2^4) = \sigma_{SB} A_1 \varepsilon_1 (T_1^2 + T_2^2)(T_1 + T_2)(T_1 - T_2) \tag{50}$$

$$\dot{Q}_{12} \approx \sigma_{SB} A_1 \varepsilon_1 (4T_m^3)(T_1 - T_2) \tag{51}$$

$$\text{where } T_m = \frac{T_1 + T_2}{2}$$

Following (51), radiative heat transfer can be modeled in terms of a thermal circuit model in which the radiative thermal resistance is given by (52).

$$R_{t,rad} = \frac{1}{4\sigma_{SB} A_1 \varepsilon_1 T_m^3} \tag{52}$$

$$\text{where } T_m = \frac{T_1 + T_2}{2}$$

The thermal resistance due to emission of radiant energy emitted from the top and bottom surfaces of the plate is given by (53). $R_{t,rad}$ is highly dependent on the temperature of the plate. In this analysis we will assume that the temperature of the plate is 10 Kelvin above ambient temperature. The emissivity of polyimide is assumed to be 1 to obtain a conservative estimate of the radiative losses.

$$R_{t,rad} = \frac{1}{4 \cdot \sigma_{SB} \cdot SA_{plate} \cdot \varepsilon_{PI} \cdot \left(\frac{T_{plate} + T_{amb}}{2} \right)^3} = \frac{1}{4 \cdot (5.67e-8) \cdot 2 \cdot (1.875mm)^2 \cdot \left(\frac{308K + 298K}{2} \right)^3}$$

$$= 2.3e4 \frac{K}{W} \tag{53}$$

3.3.1.4 Calculation of Total Thermal Resistance

Finally, we calculate the total lumped element thermal resistance by computing the parallel combination of the thermal resistance from conduction through the tethers, conduction through the air, and radiation.

$$R_t = R_{t,total} = \frac{1}{\frac{1}{R_{t,cond,4tethers}} + \frac{1}{R_{t,cond,air}} + \frac{1}{R_{t,rad}}} = 3.3e3 \frac{K}{W} \tag{54}$$

The effect of temperature on the thermal resistance is shown in Figure 3.7. The radiation resistance is temperature dependent while the conduction resistances through air and tethers are constant. The total lumped element thermal resistance is largely dominated by conduction through the air in the temperature range of interest when the calorimeter operates at atmospheric pressure. The tether conduction resistance is approximately two orders of magnitude higher than the radiation resistance. Hence, we expect the heat transfer through the tethers to be minimal.

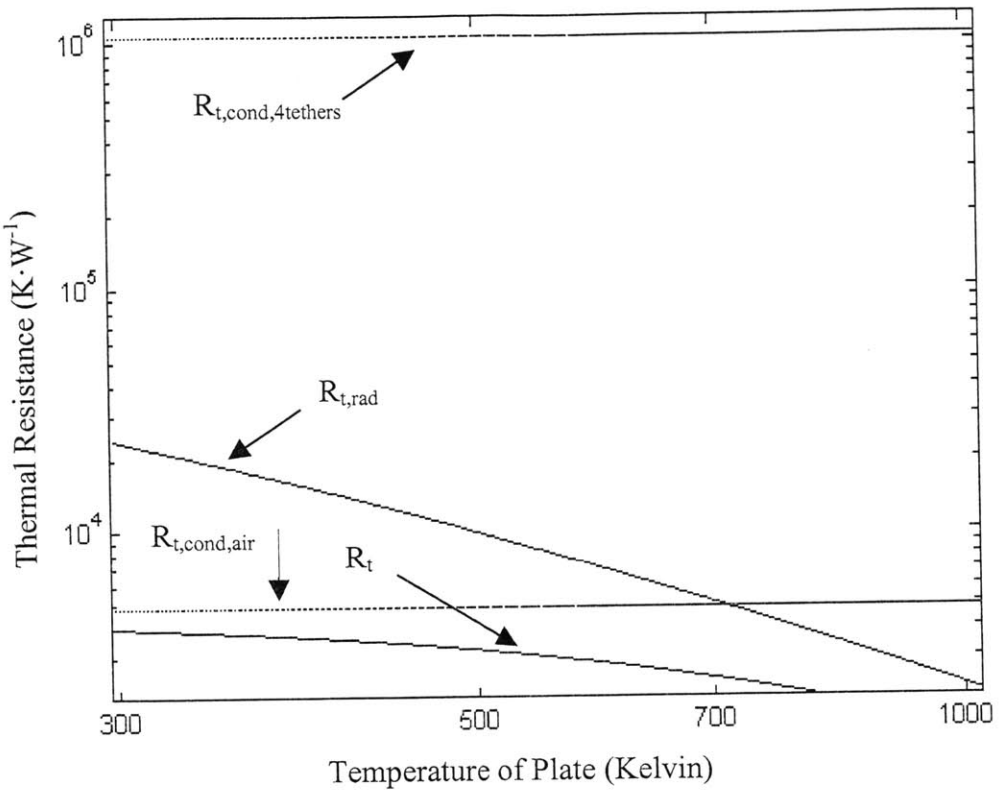

Figure 3.7. Thermal Resistances as a Function of Temperature.

3.3.2 Lumped Element Thermal Capacitance

The lumped element thermal mass is represented by capacitance C_t. The thermal capacitance of the calorimeter plate is calculated in (52).

$$C_{t,plate} = \rho_{PI} V_{PI} C_{PI} = 1390 \frac{kg}{m^3} \cdot (1.875mm)^2 \cdot 5\mu m \cdot 1088 \frac{J}{kg \cdot K} = 2.7e-5 \frac{J}{K} \qquad (52)$$

where $C_{t,plate}$ is thermal capacitance of polyimide plate
ρ_{PI} is the mass density of polyimide
V_{PI} is the volume of the polyimide plate
C_{PI} is the constant volume specific heat of polyimide

The thermal capacitance of a sample, $C_{t,sample}$, is determined similarly. The total lumped element capacitance is the sum of the thermal mass of the plate and the thermal mass of the sample (53).

$$C_t = C_{t,plate} + C_{t,sample} \tag{53}$$

3.3. 3 Summary of Lumped Element Time Constant Analysis

Table 3.2 summarizes the lumped element time constant analysis by presenting the time constants for all device geometries with tethers. The only factor that varies between these geometries is conduction through the tethers. However, the total lumped element thermal resistances for these four geometries are approximately identical because the thermal resistance is dominated by conduction through air and by radiation. Air conduction and radiation are assumed to be independent of the tether geometry in this first-order model. The thermal capacitance reflects the thermal mass of the plate alone.

Table 3.2. Lumped Element Thermal Circuit Parameters for Different Device Geometries Operating in Air. Values assume device operates in stagnant air at atmospheric pressure. The calorimeter plate is assumed to be 10 K above ambient temperature.

Tether Geometry		Lumped Element Thermal Circuit Parameters					
Length [μm]	Width [μm]	$R_{t,tethers}$ [K/W]	$R_{t,air}$ [K/W]	$R_{t,rad}$ [K/W]	$R_{t,total}$ [K/W]	C_t [J/K]	τ_e [mSec]
2790	35	1.1e6	3.9e3	2.3e4	3.3e3	2.7e-5	87
2790	95	1.1e6	3.9e3	2.3e4	3.3e3	2.7e-5	87
1403	95	5.3e5	3.9e3	2.3e4	3.7e3	2.7e-5	87
2790	300	8.9e5	3.9e3	2.3e4	3.7e3	2.7e-5	87

3.3.4 Effects of Purge Gas on Time Constant

Here, we explore the option of operating the calorimeter in stagnant argon at room temperature. Argon is chosen because it is an inert gas. Furthermore, the thermal conductivity of argon at room temperature and atmospheric pressure is about 33% lower than the thermal conductivity of air under the same conditions. Therefore, the argon conduction resistance will be higher than the air conduction resistance. Consequently, total lumped element thermal resistance and time constant also increase. The lumped

element parameters for different device geometries operating in argon are given in Table 3.3

Table 3.3. Lumped Element Thermal Circuit Parameters for Different Device Geometries Operating in Argon. Values assume device operates in stagnant argon at atmospheric pressure. The plate temperature is assumed to be 10 K above ambient temperature.

Tether Geometry		Lumped Element Thermal Circuit Parameters					
Length [μm]	Width [μm]	$R_{t,tethers}$ [K/W]	$R_{t,argon}$ [K/W]	$R_{t,rad}$ [K/W]	$R_{t,total}$ [K/W]	C_t [J/K]	τ_e [mSec]
2790	35	1.1e6	5.6e3	2.3e4	4.6e3	2.7e-5	123
2790	95	1.0e6	5.6e3	2.3e4	4.6e3	2.7e-5	123
1403	95	5.3e5	5.6e3	2.3e4	4.6e3	2.7e-5	123
2790	300	8.9e5	5.6e3	2.3e4	4.6e3	2.7e-5	123

3.4 Conclusions and Future Work

The analysis in this chapter shows that, τ_{plate}, the time constant for the plate to equilibrate with the reaction is must faster than τ_e, the time constant for the plate to equilibrate with the environment. The calorimeter must be designed such that τ_e, is much larger than the reaction time constant. As shown in Figure 3.1, we would like τ_e to be on the order of 10 seconds. In room air at atmospheric pressure, τ_e is dominated by air conduction and is estimated to be approximately 87 milliseconds. We observed that operating in a medium with lower thermal conductivity, such as argon, increases the time constant for equilibrium with the environment. In the next chapter, we measure the thermal parameters experimentally and operate the calorimeter in vacuum. Operating in vacuum also causes the thermal conductivity of air to decrease. Hence, we expect τ_e to increase in vacuum.

The analytical model derived here can be enhanced by developing a finite element model. This model could be used to capture the heating of the plate, conduction through

the tethers, conduction through the air, and radiation effects. In addition, it can be used to determine the effect of dispensing a droplet on the calorimeter plate.

Chapter 4:

Electronics

To experimentally determine the thermal model parameters of the system, a special low noise current source and amplifier were designed. The electronics were designed by Keith Baldwin and Tom King at Draper Laboratory. The same electronics could also be used to perform open-loop isothermal titration calorimetry experiments in which the calorimeter is in thermal equilibrium with the ambient. Experimental data was captured using a data acquisition routine created with a LabView interface and a16-bit analog to digital (A/D) converter from National Instruments.

4.1 Circuit Design

The temperature readout circuit shown in Figure 4.1 is designed to generate an output voltage signal, V_{out}, that is proportional to ΔT, the temperature difference between the calorimeter plate and the ambient environment.

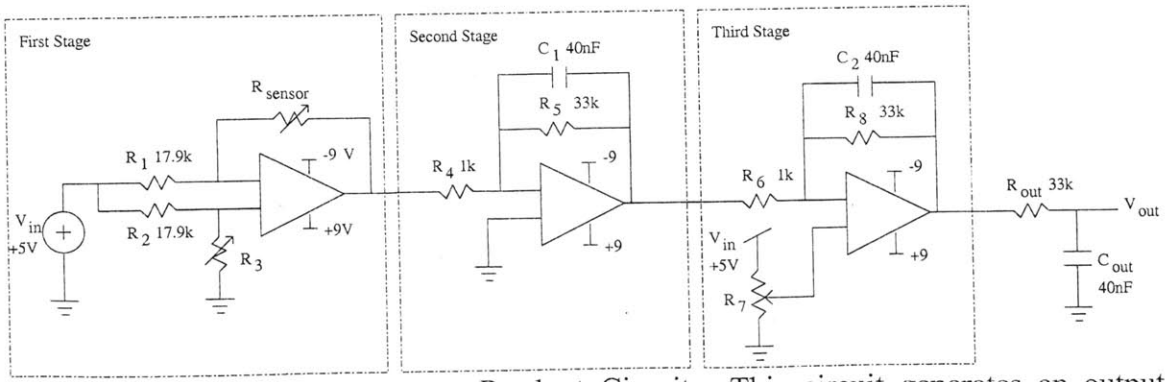

Figure 4.1. Analog Temperature Readout Circuit. This circuit generates an output voltage signal that is linearly proportional to the temperature difference between the calorimeter plate and ambient environment.

When the calorimeter is in thermal equilibrium with the ambient, the circuit is tuned to generate an output of 0 volts. The temperature of the calorimeter plate is sensed with a platinum resistor. The relationship between the resistance of the sensor and its temperature is given in (1). Parameters R_0 and α were determined empirically through a calibration experiment.

$$R_{sensor} = R_0(1 + \alpha\Delta T) \tag{1}$$

where $\Delta T = T_{plate} - T_{amb}$

R_{sensor} is the sensor resistance in Ohms at temperature T_{plate}
R_0 is the sensor resistance in Ohms at $T=T_{amb}$, or at $\Delta T=0$
α is the temperature coefficient of resistance (TCR) in $°C^{-1}$
T_{plate} is the temperature of the plate in °C
T_{amb} is the ambient temperature in °C

The resistance of the sensor, R_{sensor}, is determined by driving a known current through the resistor and measuring the voltage generated across it. By using Ohm's law, the resistance of the sensor can then be determined. Biasing the sensor resistor with a constant current, I, generates a voltage across the sensor given by (2). This results in an affine relationship between the voltage across the sensor and the temperature of the sensor.

$$V_{sensor} = IR_{sensor} = IR_0 + \alpha IR_0\Delta T \tag{2}$$

The first term in (2) is a DC offset voltage that reflects the ambient temperature. This DC offset must be nulled so only the term that varies linearly with the temperature difference between the calorimeter plate and ambient is measured. The DC offset is nulled in the first stage of the circuit. The second and third stages are cascaded gain stages that amplify the output of the first stage.

The first stage of the circuit is shown in Figure 4.2.

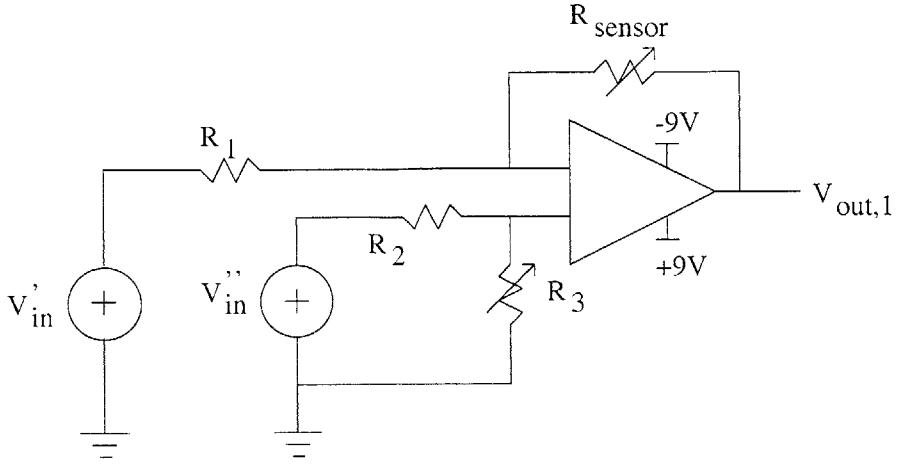

Figure 4.2. First Stage of Temperature Readout Circuit. This stage produces an output voltage signal that varies linearly with the temperature difference between the calorimeter plate and the ambient.

The transfer function for the first stage is derived using superposition. First, we determine the output of this stage when $V_{in}^{''}$ is shorted to ground as shown in Figure 4.3.

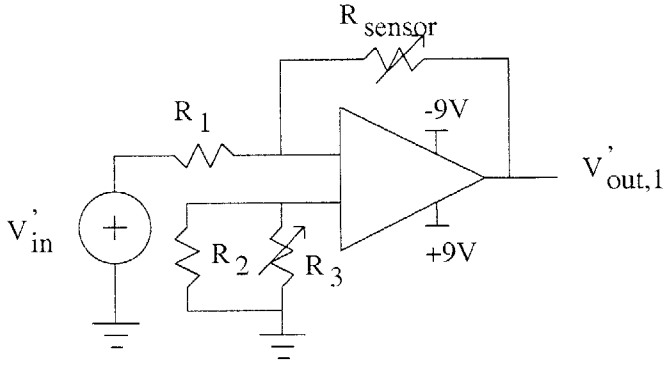

Figure 4.3. First Stage with $V_{in}^{''}$ Shorted to Ground.

By using the ideal op-amp model and ignoring the bias current into the inverting terminal of the op-amp, the current through R_{sensor} is $\frac{V_{in}^{'}}{R_1}$. Driving a constant current through R_{sensor} generates the output, $V_{out,1}^{'}$, given in (3). Substituting (1) into (3) yields (4). Equation 4 can be decomposed into two components. One component is a signal that

varies linearly with ΔT, the temperature difference between the plate and ambient. This signal is superimposed on the second component, a relatively large, negative DC voltage produced by biasing the sensor with a constant current.

$$V'_{out,1} = \frac{-R_{sensor}}{R_1} \cdot V'_{in} \tag{3}$$

$$V'_{out,1} = \frac{-R_{sensor}}{R_1} \cdot V'_{in} = -\frac{V'_{in}}{R_1} \cdot R_0 \cdot \alpha \cdot \Delta T - \frac{V'_{in}}{R_1} \cdot R_0 \tag{4}$$

To null the DC term in (4), another DC voltage is introduced at the non-inverting input of the op-amp to produce a signal of equal magnitude and opposite polarity at the output of the first stage. To understand this nulling effect, we analyze the output of the first stage when V'_{in} is shorted as shown in Figure 4.4.

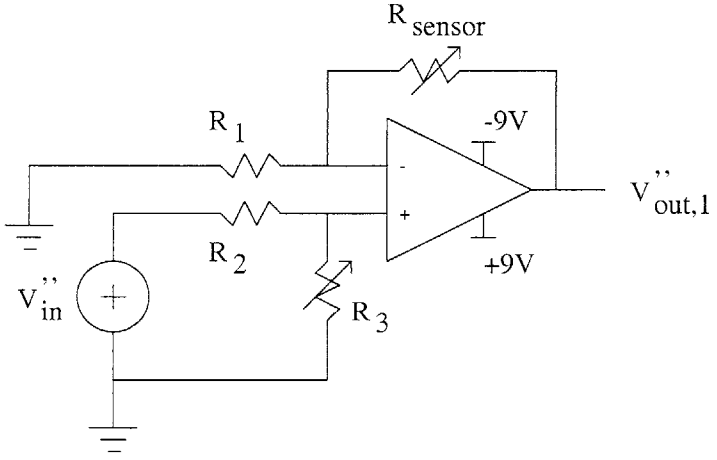

Figure 4.4. First Stage with V'_{in} Shorted to Ground.

The resulting output is given in (5). Substituting (1) into (5) yields (6)

$$V''_{out,1} = (1 + \frac{R_{sensor}}{R_1}) \cdot (\frac{R_3}{R_2 + R_3}) \cdot V''_{in} \tag{5}$$

$$V''_{out,1} = \frac{V''_{in} \cdot R_3}{R_1 \cdot (R_2 + R_3)} \cdot (R_0 \cdot \alpha \cdot \Delta T) + \frac{V''_{in} \cdot R_3}{R_2 + R_3} \cdot (1 + \frac{R_0}{R_1}) \tag{6}$$

The signal in (6) can be decomposed into two components. One component is a signal that varies linearly with the temperature difference between the plate and the ambient. The other component is proportional to the ambient temperature. Combining (4) and (6) gives the total output of the first stage. With the appropriate choice of resistors R_2 and R_3, the positive DC offset in (6) can be tuned to cancel the negative DC offset in (4). Resistor R_2 is chosen to match the resistance of R_1 and R_3 is trimmed to match R_0. Both R_1 and R_2 were set to 17.9kΩ. R_3 was constructed with a 10-turn 1kΩ potentiometer placed in series with a 500Ω fixed resistor. The potentiometer is adjusted before each use to ensure that the output of the first stage is 0 volts when the calorimeter is in thermal equilibrium with the ambient. After the first stage is tuned with the potentiometer, and all DC offsets are nulled, the effective transfer function of the first stage given in (7).

$$V_{out,1} = V'_{out,1} + V''_{out,1} = -\frac{V_{in}}{R_1} \cdot \frac{R_2}{(R_2 + R_3)} \cdot R_0 \cdot \alpha \cdot \Delta T \qquad (7)$$

For simplicity, V_{in}, V'_{in}, and V''_{in} are shown as a DC voltage sources. In the actual implementation they are realized using a 5-volt precision voltage reference chip cascaded with a low-pass filter and follower stage. The single-pole RC low-pass filter is used to band-limit the noise of the voltage reference to 100Hz. Due to the large resistance of the resistor in the RC filter, a buffer stage is required for isolation. The buffer is shown in Figure 4.5 and implemented with a non-inverting, unity gain op-amp circuit commonly known as a follower.

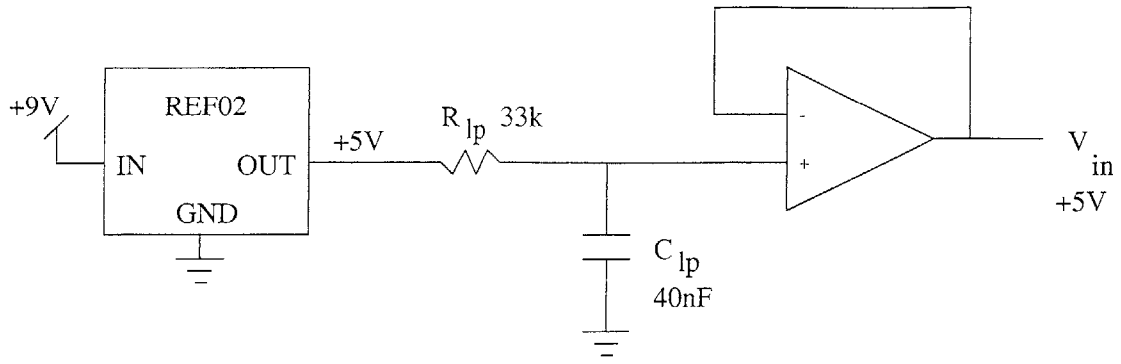

Figure 4.5. Input to First Stage of Circuit. The DC voltage sources labeled V_{in}, V_{in}', and V_{in}'' in the previous figures are realized with a 5 volt precision voltage reference chip, single pole RC filter, and follower stage as shown in the diagram.

The second stage is shown in Figure 4.6. It is a standard inverting op-amp gain stage that amplifies the output of the first stage by a factor of 33. The capacitor in parallel with the feedback resistor bandlimits the noise to 100Hz. The OP27 low noise op-amp is used in all stages to limit noise introduced by the electronics.

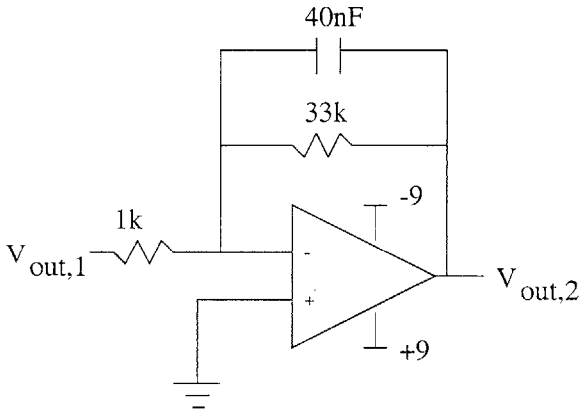

Figure 4.6. Second Stage of Circuit. This stage amplifies the output of the first stage by a factor of 33.

The third stage is shown in Figure 4.7. This stage has two functions. It amplifies the output of the second stage by a factor of 33 and nulls any offset voltage signals that have accumulated from previous stages. The voltage at the positive input can be adjusted

with a trim potentiometer to calibrate and null the output of the circuit. The capacitor in the feedback path is again used to bandlimit noise.

Finally, the output of the third stage, $V_{out,3}$, is filtered with a single pole RC lowpass filter with a 100Hz corner frequency to bandlimit noise.

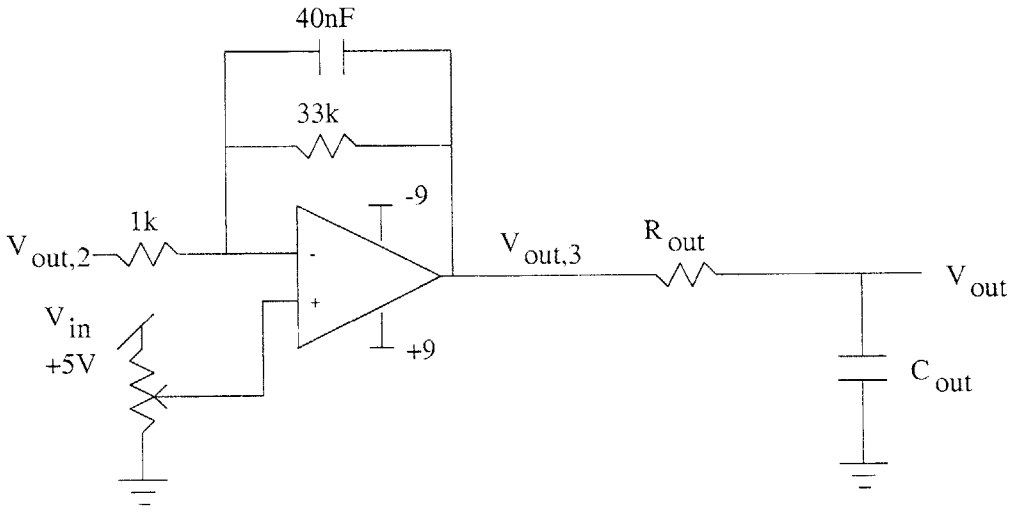

Figure 4.7. Third Stage of Circuit and Output Filter. This stage amplifies the output of the second stage by a factor of 33. The potentiometer is used to tune the circuit and null the output voltage when the plate is in thermal equilibrium with the ambient.

To summarize, the first stage of the circuit produces a signal that is linearly proportional to the temperature difference between the plate and the ambient. The second and third stages effectively amplify the output from the first stage by a factor of 1000. The transfer function between the output voltage, V_{out}, and temperature change, ΔT, is given in (8).

$$\frac{\partial V_{out}}{\partial T_{plate}} = \frac{\partial V_{out}}{\partial R_{sensor}} \cdot \frac{\partial R_{sensor}}{\partial T_{plate}} = [-1000 \cdot \frac{R_2}{R_1 \cdot (R_2 + R_3)} \cdot V_{in}] \cdot (\alpha \cdot R_0) \qquad (8)$$

4.2 Data Acquisition

Experimental data is captured using a data acquisition routine created with a 16-bit analog to digital (A/D) converter and LabView interface. The dynamic range of the

A/D converter and the sample rate can be selected at run time to maximize the resolution of the measurements. Alternatively, the data can be acquired with a digital oscilloscope.

Chapter 5:

Experimental Measurement of Thermal Model Parameters

Step response measurements are performed to experimentally determine the calorimeter's thermal model parameters. The parameters of interest are thermal resistance, thermal capacitance, and equilibrium time constant with the environment. The results of the measurements are compared to the analytical thermal model developed in Chapter 3. The circuitry used to perform the measurement is described in Chapter 4.

5.1 Extraction of Thermal Parameters Through Step Response

This section describes how a step response measurement can be used to experimentally determine the lumped element thermal model parameters described in Chapter 3.

The calorimeter is assumed to be a first-order system. The lumped element thermal circuit representation of the calorimeter is shown in Figure 5.1.

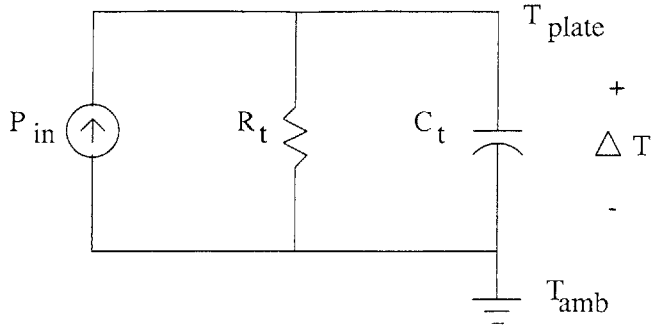

Figure 5.1. Lumped Element Circuit Representation of Calorimeter. P_{in}, R_t, and C_t represent input power, thermal resistance, and thermal mass, respectively. ΔT is the temperature difference between T_{plate}, the plate temperature and T_{amb}, the ambient temperature.

Using nodal analysis to examine the lumped element circuit, a differential equation is derived to describe the change in plate temperature as a function of time. In this chapter, τ, will be used to denote the time constant associated with the equilibration of the plate with the environment.

$$P_{in}R_t = \Delta T(t) + R_t C_t \frac{d\Delta T(t)}{dt} = \Delta T + \tau \frac{d\Delta T(t)}{dt} \quad (1)$$

$$\Delta T = T_{plate} - T_{amb} \quad (2)$$

wherer P_{in} is power input in Watts
R_t is thermal resistance in $K \cdot W^{-1}$
C_t is thermal capacitance in $J \cdot K^{-1}$
ΔT is change in plate temperature in Kelvin
T_{plate} is the temperature of the plate in Kelvin
T_{amb} is the ambient temperature in Kelvin

The response of the plate to a step power input is determined by solving the differential equation in (1). Applying a step power input at time t=0 heats the plate as shown in (3) and in Figure 2.

$$\Delta T(t) = P_{in}R_t \cdot [1 - \exp(\frac{-t}{\tau})] \quad (3)$$

Different features of the step response described by (3) and Figure 2 can be used to extract the thermal model parameters independently. The time constant, τ, can be

determined by finding the time required for the step-response to reach 63% of its steady state value, $\Delta T_{ss,heating}$. The thermal resistance is related to the steady state temperature rise, $\Delta T_{ss,heating}$, and the power input, P_{in}, as shown in (5). The thermal capacitance, C_t can be related to the initial slope of the step response curve as described by (6).

$$\Delta T(t=\tau) = \Delta T_{ss,heating}\left[1-\exp(-\frac{\tau}{\tau})\right] = \Delta T_{ss,heating}\cdot 0.63 \tag{4}$$

$$R_t = \frac{\Delta T_{ss,heating}}{P_{in}} \tag{5}$$

$$C_t = P_{in}\cdot\left[\frac{d\Delta T}{dt}\Big|_{t=0}\right]^{-1} \tag{6}$$

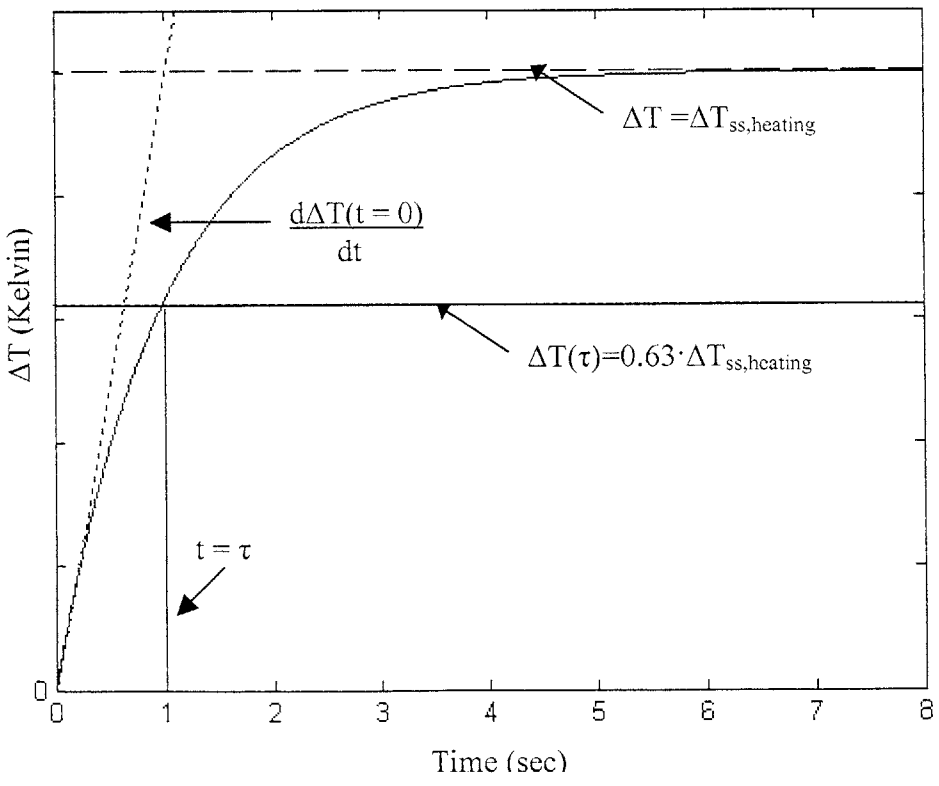

Figure 5.2. Step Response of Calorimeter Plate. Applying a step power input to the calorimeter heats the plate as shown in this figure. The smooth exponential curve is the step response. Features of the step response used to derive the thermal model parameters are identified.

Once $\Delta T_{ss,heating}$, the steady-state temperature change is reached, at some time $t_1 >> \tau$, the step power input is turned off. This enables us to observe the temperature of the plate as it relaxes back down to the ambient temperature. The cooling of the plate is expressed in (7). The characteristic time constant associated with the cooling is identical to the time constant associated with heating because the calorimeter is a first-order system.

$$\Delta T(t) = \Delta T_{ss,heating} \cdot \exp[\frac{-(t-t_1)}{\tau}] \tag{7}$$

The time constant can be determined by finding the time required for the temperature change to decrease 37% from its value at time t = t1, as shown in (8).

$$\Delta T(t = t_1 + \tau) = \Delta T_{ss,heating}\left[\exp(-\frac{\tau}{\tau})\right] = \Delta T_{ss,heating} \cdot 0.37 \tag{8}$$

The thermal resistance and capacitance are extracted as described in (9) and (10).

$$R_t = \frac{\Delta T_{ss,heating}}{P_{in}} \tag{9}$$

$$C_t = P_{in} \cdot \left[\frac{d\Delta T}{dt}\Big|_{t=t_1}\right]^{-1} \tag{10}$$

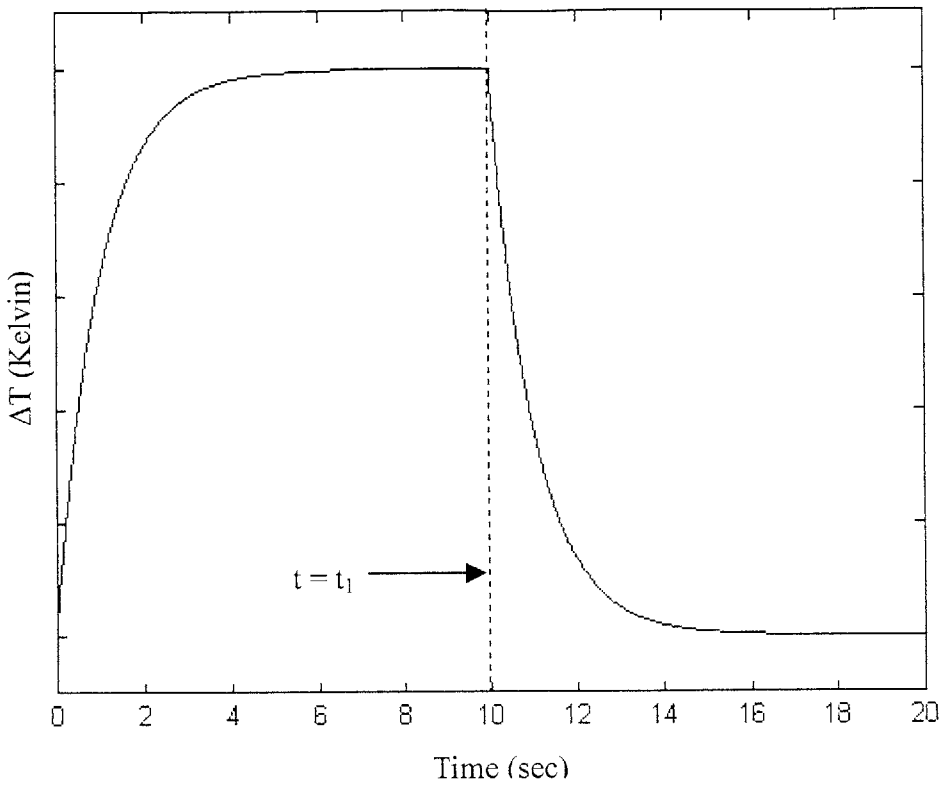

Figure 5.3. Response of Plate Temperature when Power Input is Turned Off at $t=t_1$.

5.2 Experimental Set-Up

This section describes the experimental set-up used to perform the step response measurement.

Each packaged device is placed into a chip socket and then placed in a bell jar which is connected to a vacuum system. SMA connectors are used to connect the device's sensor resistor to the readout circuit, which is external to the bell jar. SMA and BNC connectors are used to connect the device's heater resistor to the signal generator, which is also external to the bell jar. The signal generator is used to create the step power input. The output voltage signal of the temperature readout circuit is connected to a LabView data acquisition unit.

At time t=0, a step input of power is applied to the calorimeter. The step power input is generated by applying a voltage step with amplitude V_{step} across R_h, the calorimeter's heater resistor as shown in Figure 5.4.

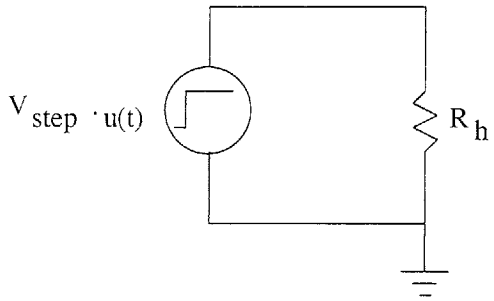

Figure 5.4. Voltage Step Across the Heater Resistor Generates a Step Power Input to the Calorimeter. u(t) is a unit step function. The voltage input, V_{step}·u(t), is a step with amplitude V_{step}.

The magnitude of the power input is given in (11). The heater resistance, R_h, is assumed to remain constant. Resistance changes due to self-heating are neglected.

$$P_{in} = \frac{V_{step}^2}{R_h} \tag{11}$$

The power input to the calorimeter raises the temperature of the calorimeter's plate. The temperature change is sensed by a platinum resistive temperature detector. The circuit described in Chapter 4 reads the resistance of the sensor and produces an output voltage signal that is proportional to the temperature difference between the plate and ambient. This analog output voltage signal is sampled at discrete points in time and digitally stored using a LabView data acquisition unit. The data captured during the measurement is in units of volts and must be scaled according to the relationship shown in Equation (8) of Chapter 4 to determine temperature.

Once the raw data is post-processed to determine the temperature change of the plate as a function of time, Origin software is used to fit the data to an exponential curve.

For the data corresponding to heating, a Box Lucas fit is used. It fits the data to the generic exponential expression shown in (12). The time constant and steady state temperature rise are extracted easily from the curve fit. The thermal capacitance is determined by applying (6). The thermal resistance is determined by dividing the time constant by the thermal capacitance.

$$y(x) = a[1 - \exp(-bx)] \tag{12}$$

where x corresponds to time, t
y corresponds to temperature change, ΔT
a corresponds to $\Delta T_{ss,heating}$
b corresponds to $\frac{1}{\tau}$

5.3 Experimental Test Conditions and Hypothesized Results

One device of each geometry is tested under various conditions as described in this section. Devices with tethers that measure 35μm in width and 2790μm in length could not be tested as they were depleted in other characterization studies.

The vacuum system is used to perform step response measurements on each device over a range of pressures from 1mTorr to 760Torr (atmospheric pressure). The range of pressures is limited by the capabilities of the vacuum pump. As shown in by the lumped element model in Chapter 3, the dominant heat transfer mechanism at atmospheric pressure is air conduction. The thermal conductivity of air varies as a function of the pressure inside the bell jar. Varying the pressure inside the bell jar with the vacuum system will allow us to characterize the power losses caused by other heat transfer mechanisms as the effects of air conduction diminish at low pressures. The power input is varied to yield roughly the same temperature change for each set of measurements taken using a particular device. This keeps the contribution from radiation constant.

The thermal conductivity of air varies with pressure. This behavior can be explained through the kinetic theory of gases. The thermal conductivity of air is dependent on its mean free path, λ_m. The mean free path is defined as the distance a molecule can travel before colliding with another molecule. The mean free path of air is strongly dependent on pressure as shown in (13) [16].

$$\lambda_{m,air} = (1.4e-6)\cdot\frac{T}{P} \tag{13}$$

where $\lambda_{m,air}$ is the mean free path of air in centimeters
T is the temperature in Kelvin
P is the pressure in Torr

The ratio of the mean free path and the characteristic dimension D, which represents the gap between the calorimeter plate and the package, is known as the Knudsen number. Denoted as N_{kn}, the Knudsen number is a dimenionless quantity used to stratify different gas flow regimes. The relationship between the mean free path and thermal conductivity of air can be explained through these different flow regimes.

$$N_{kn} = \frac{\lambda_{m,air}}{D} \tag{14}$$

where N_{kn} is the dimensionless Knudsen number
$\lambda_{m,air}$ is the mean free path of air in centimeters
D is the distance between the bottom surface of the calorimeter plate and Package in centimeters.

Following [17], three gas flow regimes are considered. The first regime is the continuum flow regime in which the gas behaves as a continuous medium [17]. In this regime, the thermal conductivity of air is constant. The second regime is the slip flow regime. In this regime, the mean free path approaches the characteristic dimension, D. The velocity of the gas at the wall is no longer zero, thereby violating the "no-slip" condition. The third regime is the free molecule flow regime. In this regime, the mean free path is larger than the characteristic dimension, D. The thermal conductivity of air decreases linearly

with pressure as the collisions between air molecules occur at diminishingly low frequencies. The value of the Knudsen number is used to stratify the gas flow into these regimes as shown in Table 1. The thermal conductivity of air as a function of pressure, based on the dimensions of the calorimeter, is given in Figure 5.5. As the pressure varies between 760Torr and 1mTorr, the thermal conductivity decreases by a factor of 100.

Table 5.1. Relationship between Knudsen number, gas flow regime, and thermal conductivity of air. k_0 is the thermal conductivity of air at atmospheric pressure at temperature $T=T_0=300K$ [16] [17].

Knudsen number N_{kn}	Gas flow regime	Thermal Conductivity
$N_{kn} < 0.001$	Continuum flow	$k_{air} = k_o \cdot \left(\frac{T}{T_0}\right)$
$0.001 < N_{kn} < 2$	Slip flow	$k_{air} = \frac{k_0}{1+\frac{a}{N_{kn}}}$ where a is a constant
$N_{kn} > 2$	Free molecule flow	$k_{air} = \frac{b \cdot \sqrt{T}}{N_{kn}}$ where b is a constant

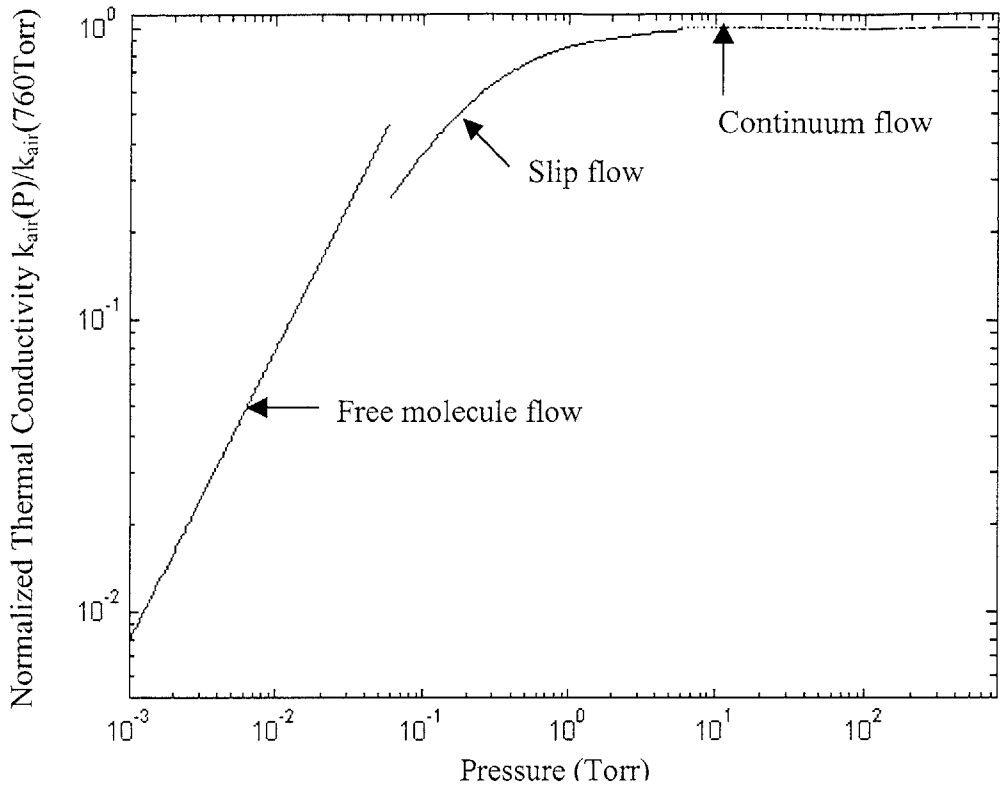

Figure 5.5. Thermal Conductivity of Air as a Function of Pressure. These curves follow [16], which gives the thermal conductivity of air at reduced pressure between infinite parallel plates with spacing D. In this scenario, D is the distance between the calorimeter plate and package. Temperature is assumed to be 300K. The horizontal axis is pressure in Torr. The vertical axis is normalized to the thermal conductivity of air at atmospheric pressure (760Torr).

From the thermal model developed in Chapter 3 and the relationship between k_{air} and pressure shown in Figure 5.5, we predict that the experiment described above, in which the pressure is varied between atmospheric pressure and 1mTorr, will cause the thermal resistance to change as shown in Figure 6. In this analysis, we assume that radiation and air conduction are the dominant heat transfer mechanisms. The steady state change in plate temperature is assumed to be 10 Kelvin. Furthermore, the air conduction and radiation terms are assumed to be dependent on the dimensions of the plate, and independent of the tether dimensions. Because all tethered devices have the same plate

dimensions, their thermal resistance values should be identical when tested under similar conditions.

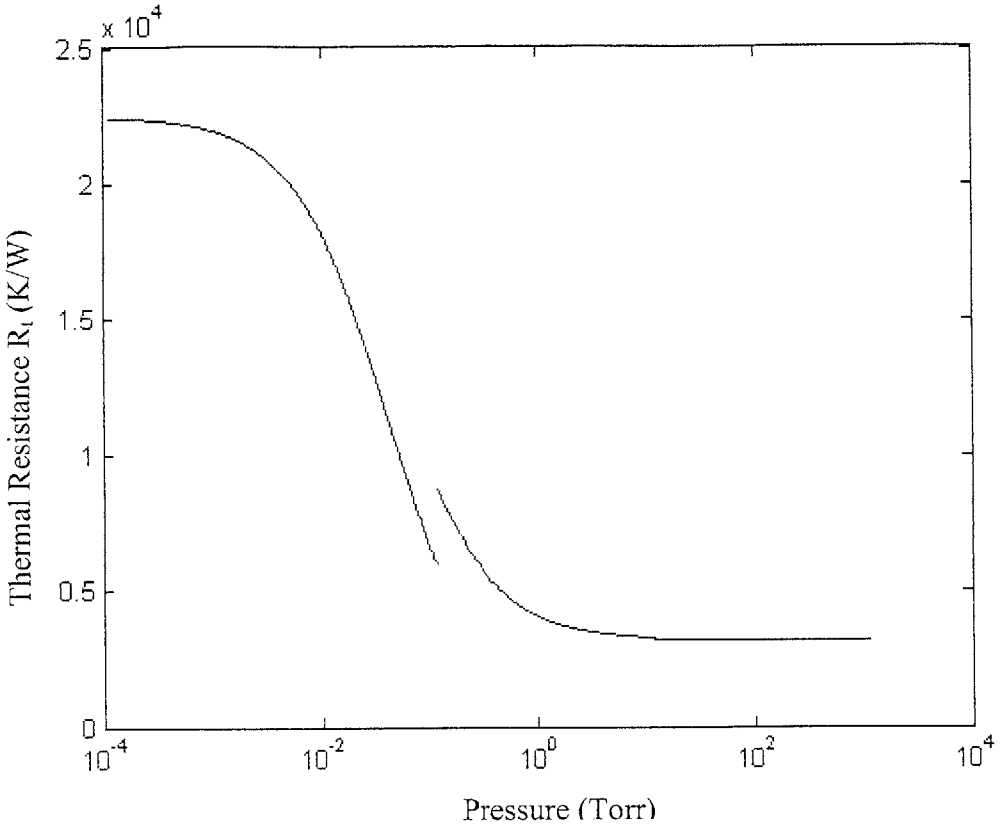

Figure 5.6. Expected Relationship between Pressure and Thermal Resistance for Devices with Tethers. This model assumes that radiation and air conduction are the dominant heat transfer mechanisms.

Figure 6 shows that the thermal resistance is fairly constant and dominated by air conduction from 760Torr down to 1Torr. In this pressure range, the average thermal resistance is approximately $3.9e3K \cdot W^{-1}$. The thermal resistance remains constant because the thermal conductivity in air is constant. The thermal resistance is a parallel combination of the resistances due to air conduction and radiation. Because the resistance due to air conduction is roughly a factor of 50 smaller than the radiation resistance, the air conduction will dominate.

From 100mTorr down to 10mTorr, the thermal resistance increases linearly as the pressure decreases. This is due to the linear variation in the thermal conductivity of air in this range.

As the pressure decreases further, the air conduction resistance becomes much larger than the radiation resistance. Therefore, the thermal resistance is dominated by radiation. Following Figure 5.6, we anticipate that the experimental results can be used to characterize the thermal resistances to air conduction and radiation. The thermal resistance to conduction through the tethers cannot be verified with these measurements.

When measuring the time constant as a function of pressure, we expect the time constant to follow the same trend as the thermal resistance. The time constant is the product of the thermal mass and thermal resistance. The thermal mass should stay constant at all pressures. Hence, any change in the time constant is attributed only to a change in the thermal resistance.

5.4 Experimental Results and Data Analysis

The data for each step response measurement is fit to an exponential using the Origin software package, as described in section 5.3. The equation for the exponential fit is used to determine the time constant. The thermal capacitance is derived using (6). The data from all measurements for a particular device is used to compute an average thermal capacitance. The time constants for each measurement are divided by the average thermal capacitance to compute the thermal resistances.

We first consider the step response measurement data for a device with tethers that measure 300μm in width and 2790μm in length. The power input was varied for each measurement to induce the same temperature change and keep the contribution from

radiation constant. The average steady state temperature rise was 9.5 Kelvin with a standard deviation of 0.3 Kelvin. Figure 5.7 shows an example of the curve fit generated by Origin overlaid on the measured data for one step response measurement taken in vacuum.

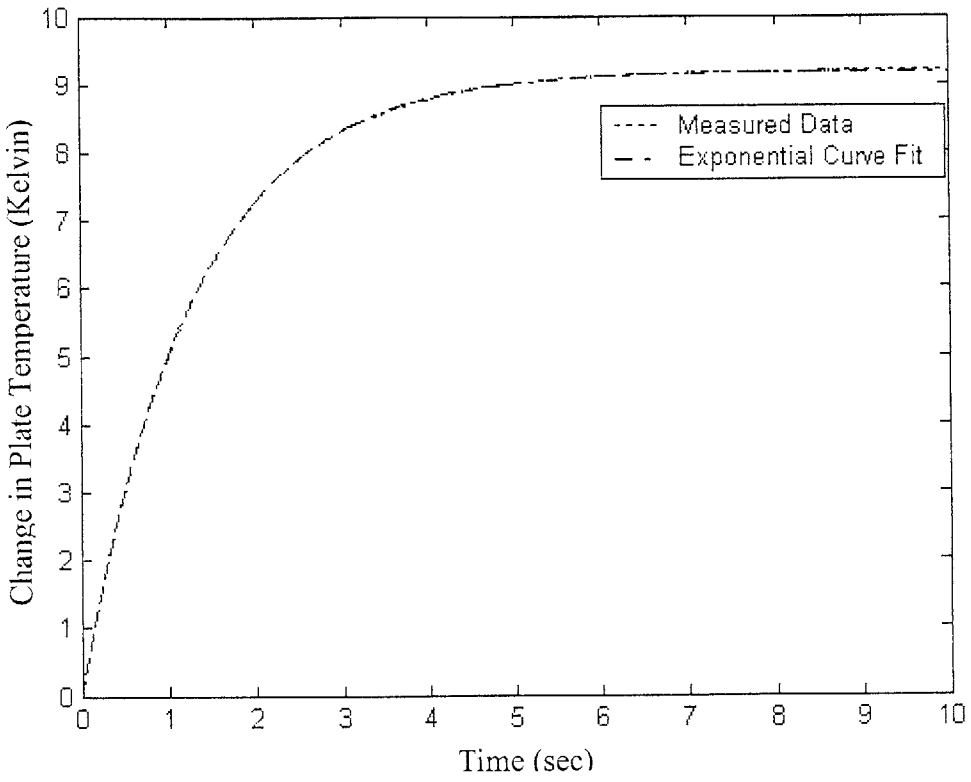

Figure 5.7. Measured Data and Curve Fit for Step Response Measurement taken in Vacuum at 1 mTorr. The exponential curve fit coincides almost perfectly with the measured data.

The results from measurements of other device geometries are summarized at the end of this section.

5.4.1 Thermal Capacitance Measurement Results

The average measured thermal capacitance of a single calorimeter device without any samples on the surface is 2.9e-5 $J \cdot K^{-1}$ with a standard deviation of 3.3e-6 $J \cdot K^{-1}$. The

calculated value for the thermal capacitance of the plate is 2.7e-5 $J \cdot K^{-1}$. These results are compiled from 26 tests performed on one calorimeter device with 300μm wide, 2790μm long tethers.

5.4.2 Thermal Resistance Measurement Results

The measured thermal resistance as a function of pressure is shown in Figure 5.8 and is plotted against the expected trend shown in Figure 5.6.

When comparing expected and measured results, we notice that the expected and measured thermal resistances follow similar trends. The measured thermal resistance stays roughly constant from 760Torr down to 1Torr. The average measured thermal resistance in this range of pressures is 3.0e3 $K \cdot W^{-1}$ with a standard deviation of 260$K \cdot W^{-1}$. The thermal model from Chapter 3 predicts that the average thermal resistance in this range is 3.9e3 $K \cdot W^{-1}$. For pressures at or below 1mTorr, the thermal resistance is dominated by radiation. The measured thermal resistance is 4.5e4$K \cdot W^{-1}$. The analytical thermal model, which assumes an emissivity for polyimide of 1, predicts that the radiation resistance should be 2.2e4 $K \cdot W^{-1}$. The discrepancy between the analytical model and the measured result can be attributed to an overestimate of the emissivity in the analytical model.

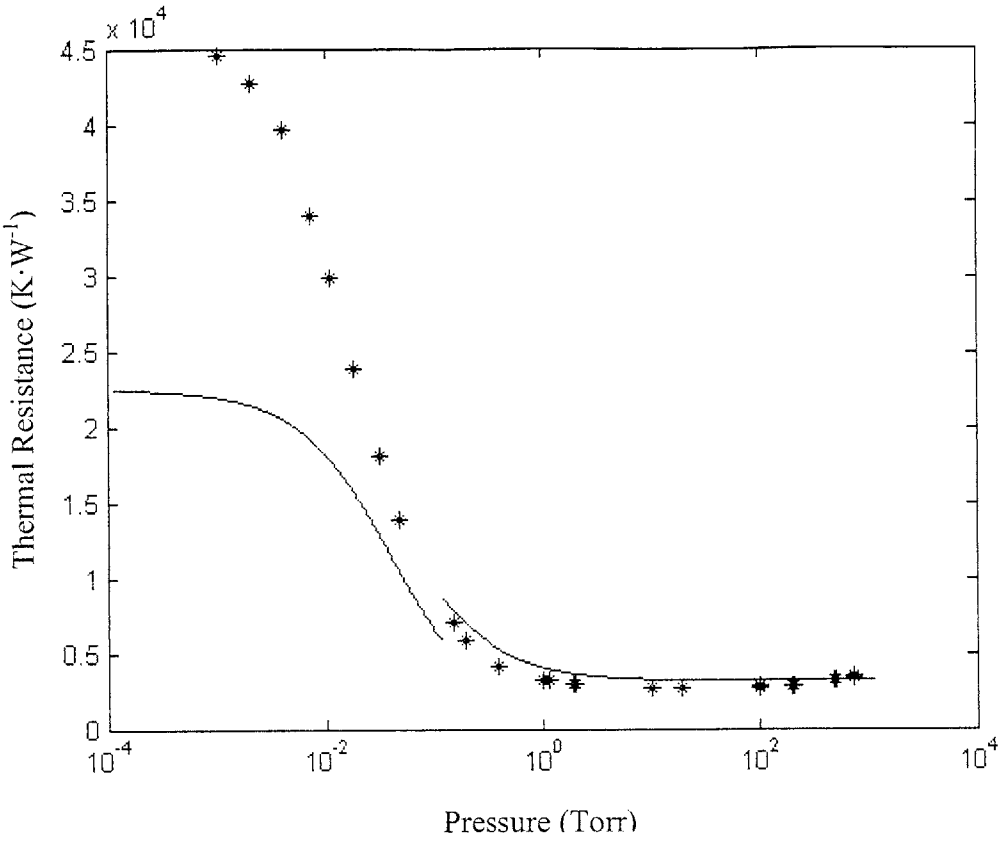

Figure 5.8. Measured and Expected Thermal Resistances as a Function of Pressure. The expected trend is represented by the discontinuous lines and the measured data is shown with asterisks. The device used in the measurement has tethers that are 95μm in width and 2790μm in length. The radiation resistance is kept constant by inducing a steady state temperature change of approximately 9.5 Kelvin for each measurement.

By decreasing the emissivity of polyimide from 1 to 0.48, we modify our thermal model to produce a model that is more consistent with the measured results. The values of the thermal resistances calculated as a function of pressure through this modified model are shown in Figure 5.9.

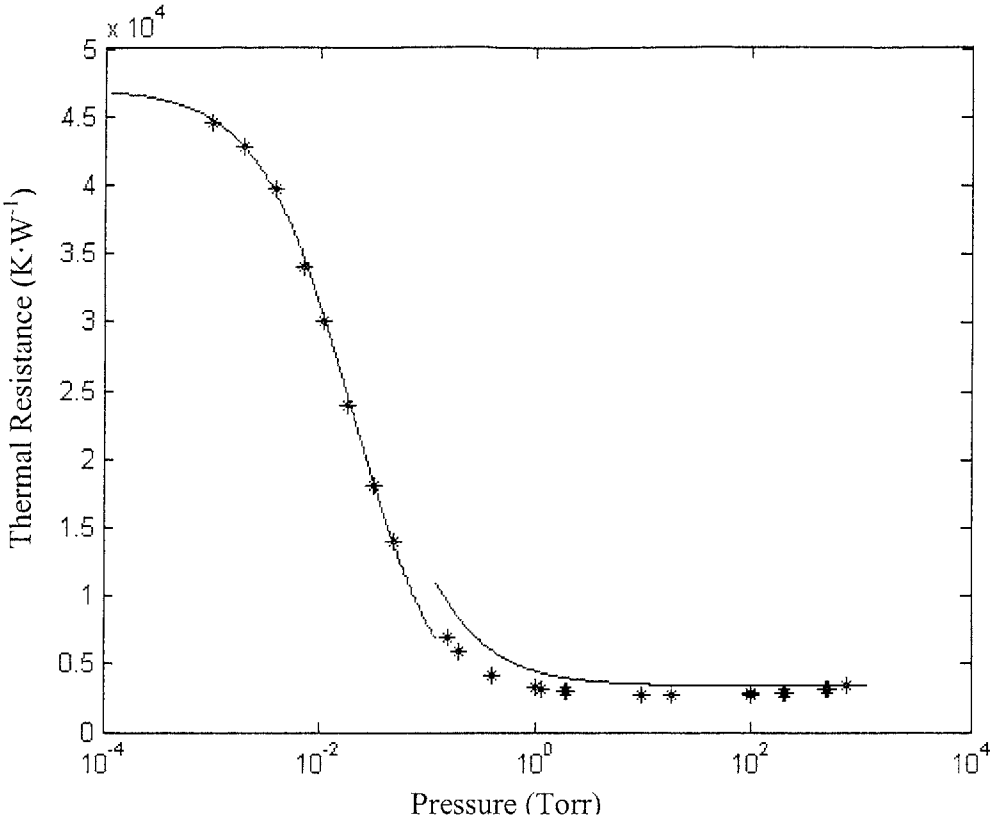

Figure 5.9. Measured and Analytic Thermal Resistances as a Function of Pressure. The asterisks represent the measured values. The emissivity of polyimide from the analytical thermal model is modified to create a model that is consistent with the measured results. The discontinuous lines are thermal resistance values calculated from the analytical model.

After modifying the thermal model, the analytical results and measured results are in good agreement in the free molecule flow regime, over a pressure range from 100mTorr down to 1mTorr. From atmospheric pressure down to 100mTorr, the measured thermal resistances are lower than those predicted by the model. In this range of pressures, the thermal resistance is dominated by air conduction, as predicted. The lumped element model only accounts for the air conduction from the surface of the plate. The air conduction from the edges of the plate and from the surface of the polyimide tethers is neglected. Adding these contributions to the thermal model may lower the analytical air conduction resistance. There is also some scatter in the data between

atmospheric pressure and 1Torr. The analytical models predict that the thermal conductivity of air is constant over this range. The measured values indicate that the thermal conductivity of air may actually increase by as much as 10% as the pressure decreases from atmospheric pressure to 1Torr.

The experimentally measured time constants for the plate to reach equilibrium with the environment are plotted versus pressure for all devices in Figure 5.10.

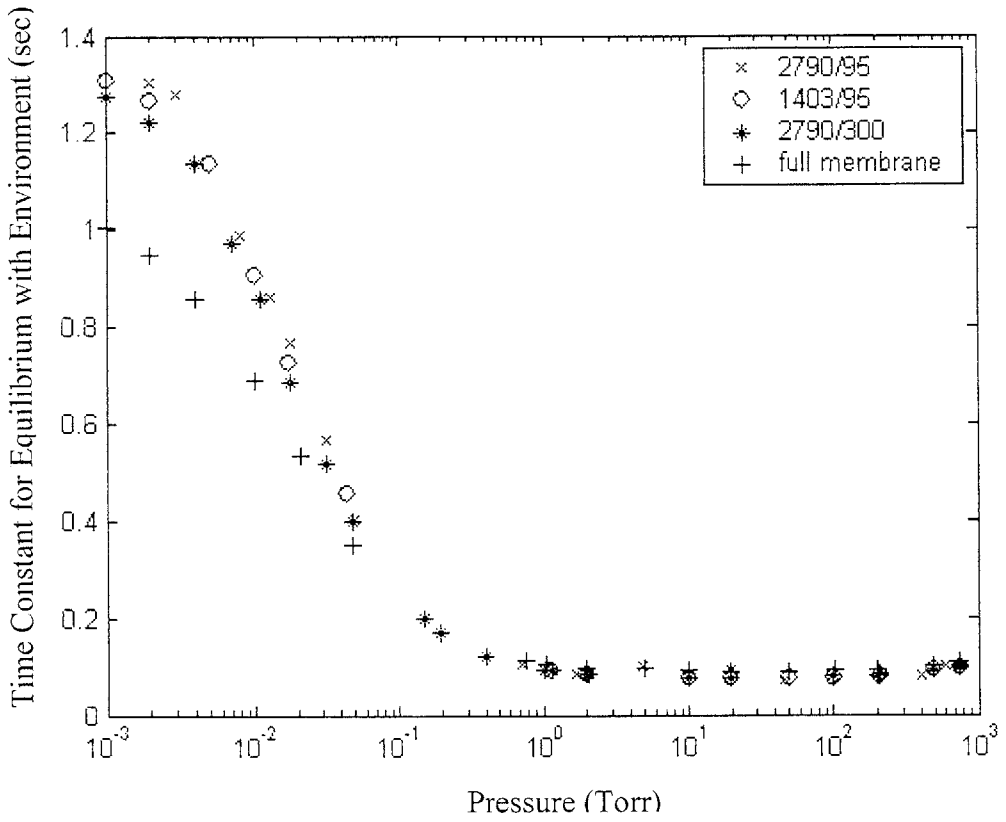

Figure 5.10. Experimentally Measured Time Constants Versus Pressure for Different Device Geometries. The legend maps the device geometries in terms of their tether lengths and widths to the data shown.

The devices with tethers behave similarly, which is consistent with the theoretical analysis. When compared to the devices with tethers, the full membrane device has lower time constants at pressures below 100mTorr. The tethered devices each have a 1.875mm x 1.875mm plate that is connected to the silicon frame by four tethers that

extend from the corners of the plate. The tethers are triple-layer structures fabricated from polyimide, titanium, and platinum. The full membrane device can be thought of as a 1.875mm x 1.875mm plate with eight tethers. Four tethers extend from the corners of the plate, just as in the previous case. The other four tethers are single-layer polyimide structures that extend from the edges of the plate. Conduction through the latter four tethers is significant because they are 1970μm long and 1875μm wide. In addition, the increased surface area of the polyimide membrane increases the radiative losses and lowers the time constant to reach equilibrium with the environment.

5.5 Conclusions and Future Work

By referring to Figure 1 of Chapter 3 and by examining the experimental results shown here, we see that the time constant for equilibration with the environment is faster than the reaction time constants. Hence, the time constant for equilibration with the environment must be increased for this calorimeter to be used in the target application.

The initial modeling of the device, prior to fabrication, assumed that the device would operate in vacuum and that the dominant heat loss mechanism would be conduction through the tethers. By varying the thermal conductivity of air through operation of the device in a vacuum system, we see that the effects of air conduction can virtually be eliminated. However, at sufficiently low pressures, the thermal losses are dominated by radiation and not by conduction through the tethers. To operate in a regime in which conduction through the tethers dominates, the radiative effects must be minimized. In vacuum, with the current calorimeter design, the radiation resistance is a factor of ten smaller than the tether conduction resistance. The radiation resistance must be increased by at least a factor of 100 to achieve a situation in which conduction through

the tethers does indeed dominate. The radiation resistance can be increased by fabricating the plate from a material of a lower emissivity or by decreasing the area of the plate. The time constant for equilibration with the environment is the product of the thermal resistance and thermal capacitance. Thus, if we increase the thermal resistance by constructing the plate from a material with lower emissivity, we would also need to consider the mass density and heat capacity of this new material and determine the effect on the thermal capacitance. If we decided to decrease the area of the plate, we would need to ensure that the volume of the plate was conserved so that the time constant does not decrease. This would require increasing the thickness of the plate. Increasing the thickness of the plate increases the time constant for the plate to equilibrate with the reaction. This plate time constant varies proportionally with the square of the plate thickness.

It is interesting to note that heat transfer in the current design is always dominated by air conduction or radiation. The thermal resistance due to each of these mechanisms varies inversely with the area of the plate. The thermal capacitance of the plate, however, varies directly with the area of the plate. The time constant for the calorimeter to equilibrate with the environment is the product of the thermal resistance and thermal capacitance. Hence, even if we increase the plate area, the time constant may stay constant because the increase in thermal capacitance will cancel the decrease in thermal resistance.

Chapter 6:

Characterization of Noise in Temperature Sensor

Inherent noise in the temperature sensor causes its apparent resistance to fluctuate, thereby limiting the sensor's ability to resolve temperature. This chapter experimentally characterizes the frequency spectrum of the noise in the resistive temperature sensor.

6.1 Analytical Noise Model

In this section, we analytically model the noise in the temperature sensor. Two potential noise mechanisms commonly associated with resistors are investigated and characterized in terms of their power spectral density functions.

Two noise mechanisms that generate noise in resistors are Johnson noise and flicker noise. Johnson noise is a form of thermal noise caused by thermal excitation of electrons in a resistor. Johnson noise is characterized as white noise because it has a uniform spectrum over all frequencies. The power spectral density of Johnson noise is given in (1).

$$V^2_{n,Johnson}(f) = 4k_B TR \tag{1}$$

where k_B is Boltzmann's constant, or 1.38×10^{-23} J·K^{-1}
T is temperature in Kelvin
R is resistance in Ohms

$V^2_{n,Johnson}(f)$ represents the average normalized noise power over a 1Hz bandwidth and is expressed in units of $\frac{V^2}{Hz}$. Following (1), we note that any two resistors with the same electrical resistance will have the same Johnson noise characteristic when held under the same temperature, regardless of the compositions of the resistors.

Flicker noise is another noise mechanism present in resistors. Flicker noise is a low-frequency phenomenon that arises whenever a DC current flows through a resistor. It is also known as "1/f" noise because its power spectral density varies inversely with frequency. A general expression for flicker noise in a resistor with resistance R, biased with DC current I, is given in (2).

$$V^2_{n,flicker}(f) = \frac{k_m I^2}{f^{\alpha}} \tag{2}$$

where k_m and α are experimentally measured coefficients
I is the DC current through resistor

The characterization of flicker noise is more complex than the characterization of Johnson noise because flicker noise varies with several factors. It is, therefore, measured experimentally. The coefficient k_m in (2), for instance, has been shown to vary with temperature, electrical resistance, and material properties [17][19]. The flicker noise is generally accepted to vary with the square of the DC current as shown in (2) [17].

The Johnson noise and flicker noise in a resistor are uncorrelated noise sources. Therefore, the total noise spectral density can be obtained by adding the contributions from the Johnson noise and flicker noise as shown in (3).

$$V_n^2(f) = V^2_{n,Johnson}(f) + V^2_{n,Johnson}(f) = 4k_b TR + \frac{k_m I^2}{f^{\alpha}} \tag{3}$$

The root spectral density, $V_n(f)$, for a noise voltage signal with flicker and Johnson noise components is shown in Figure 6.1. The root spectral density of the sensor noise is expected to have a similar shape. At low frequencies, the flicker noise dominates, and the spectral density varies inversely with frequency. At high frequencies, Johnson noise dominates. Here, we draw a dotted line tangent to the portion of the curve in which flicker noise dominates. A horizontal dashed line is used to show the noise floor created by the Johnson noise. The intersection of the dotted and dashed lines is known as the 1/f corner.

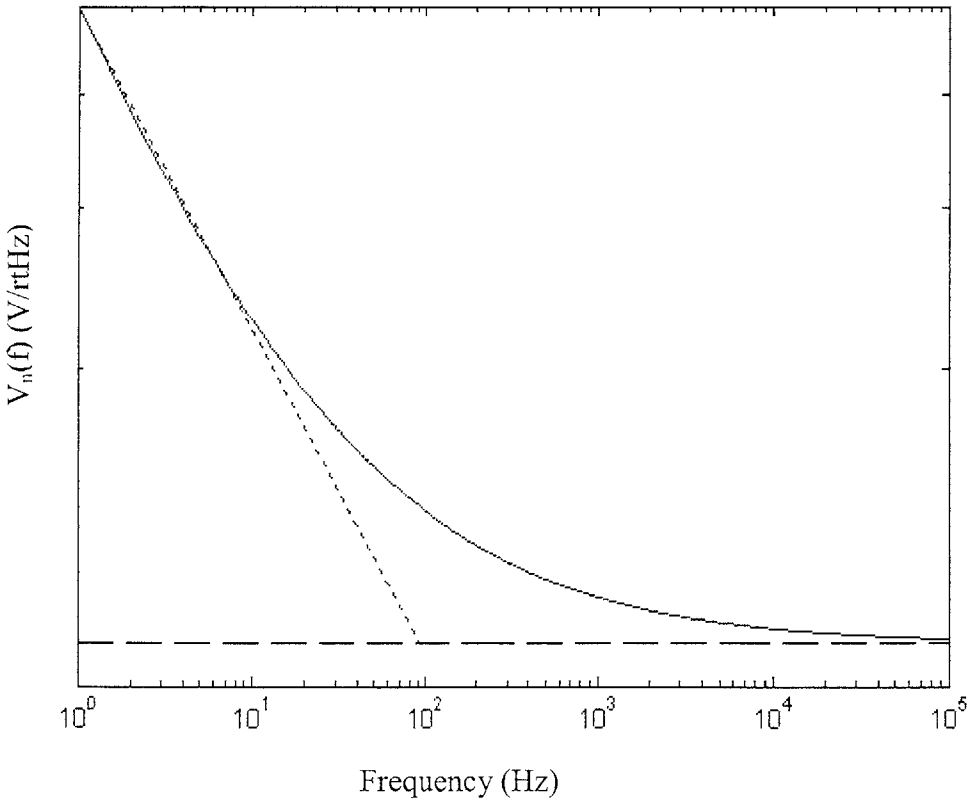

Figure 6.1. Root Spectral Density of Noise Signal with Flicker and Johnson Noise Components. The smooth curve is the root spectral density. The dotted line is the tangent to the root spectral density. The dashed line represents the Johnson noise floor. The intersections of the dotted and dashed lines is known as the 1/f corner.

Following (3), the temperature sensor can be modeled with an ideal noise-free resistor in series with a voltage source that represents the noise signal generated across the resistor. This is shown in Figure 6.2. Alternatively, the noise can be modeled as a noise-free resistor in parallel with an equivalent current noise source.

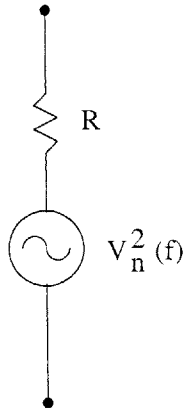

Figure 6.2. Noise Model for Resistor with Johnson Noise and Flicker Noise Components.

6.2 Experimental Noise Measurement Set-Up

In this section, we design an experiment to measure the noise characteristic of the sensor. As discussed in the previous section, noise is characterized by its power spectral density. The frequency spectrum of electrical noise can be measured over a broad frequency range with a spectrum analyzer. The spectrum analyzer used in this measurement is the HP35670A dynamic signal analyzer. The analyzer samples, digitizes, and quantizes the analog voltage signals and then uses a fast Fourier transform (FFT) algorithm to compute their power spectral density.

The Johnson noise of the sensor resistor puts a lower bound on $V_n(f)$, the resistor's voltage noise density. When measured at room temperature, the electrical resistance of the sensor used in this characterization is 1290Ω. The voltage noise density due to thermal noise is calculated for this resistor using (1) and is approximately

$4.5\frac{nV}{\sqrt{Hz}}$. When the inputs to the analyzer are shorted, the noise floor of the analyzer is measured to be $20\frac{nV}{\sqrt{Hz}}$. Therefore, the Johnson noise component cannot be measured by this analyzer unless it is amplified with sufficient gain.

The resistor noise is amplified by configuring the sensor resistor in the op-amp circuit shown in Figure 6.3. Because the resistor is placed between the non-inverting terminal and ground, the resistor noise is amplified by $1+\frac{R_F}{R_1}$. Ideally the amplification would be provided by a noise-free amplifier. However, all amplifiers, including this op-amp, add noise to the signal being amplified. The resistors used to set the gain of this op-amp circuit also contribute additional noise to the output signal, V_{no}.

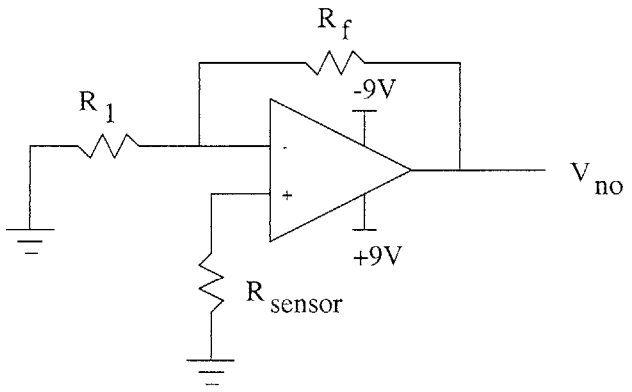

Figure 6.3. Circuit to Amplify Sensor Noise.

The characterization of the sensor noise is accomplished with two experiments. The first experiment is a control experiment that characterizes the noise of the amplifier and the resistors used to set its gain, in the absence of the sensor. The circuit used in this experiment is shown in Figure 6.4.

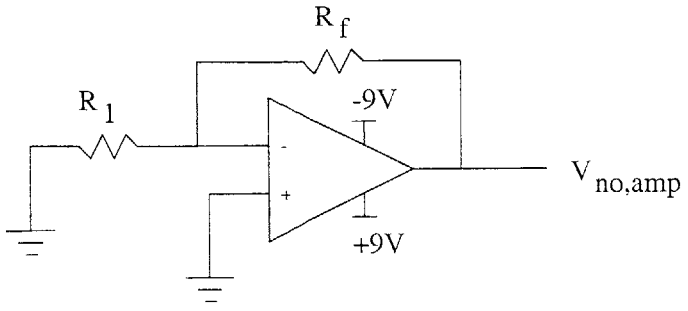

Figure 6.4. Amplifier Circuit in the Absence of Sensor.

The voltage noise density at the output of the amplifier, $V_{no,amp}(f)$, is measured with the signal analyzer. In the second experiment, the sensor resistor is inserted between the non-inverting input of the op-amp and ground as shown in Figure 6.3. The voltage noise density at the output of this circuit, $V_{no}(f)$, is also measured with the signal analyzer. Subtracting the power spectral densities measured in the two experiments allows us to characterize the excess noise produced by the sensor.

The following is an analytical model to characterize the noise contributed by the op-amp circuit and gain resistors. The noise model for the amplifier circuit is shown in Figure 6.5 [20].

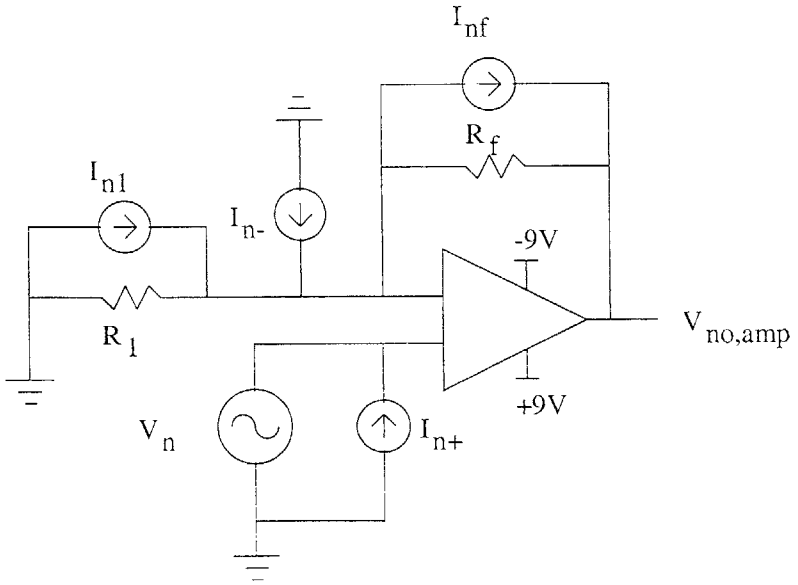

Figure 6.5. Noise Model for Amplifier Circuit and Gain Resistors.

Current sources I_{n1} and I_{nf} model noise in resistors R_1 and R_f, respectively. Current sources I_{n-} and I_{n+} model the input current noise at the negative and positive inputs of the op-amp. Voltage source V_n models the voltage noise density of the op-amp. This voltage noise of the op-amp is typically referred to its non-inverting input, consistent with the model shown Figure 6.5.

Superposition is used to determine $V_{no,\,amp}(f)$, the noise voltage at the output of the amplifier. All noise sources are assumed to be uncorrelated. We first consider the noise contribution from current sources $I_{n1}(f)$, $I_{n-}(f)$, $I_{n+}(f)$. We assume that no DC current flows through R_1. The mean-squared voltage noise at the output is shown in (4).

$$V_{no,amp,1}^2(f) = [I_{n1}^2(f) + I_{nf}^2(f) + I_{n-}^2(f)] \cdot R_f^2 \tag{4}$$

We now consider the contribution from the voltage noise source at the non-inverting input.

$$V_{no,amp,2}^2(f) = [V_n^2(f)] \cdot [1 + \frac{R_f}{R_1}]^2 \tag{5}$$

The total mean-squared voltage noise at the output of the amplifier is obtained by adding (4) and (5).

$$V_{no,amp}^2(f) = V_{no,amp,1}^2(f) + V_{no,amp,2}^2(f) \tag{6}$$

The noise model for the amplifier circuit with the sensor resistor is shown in Figure 6. Voltage source $V_{n,sensor}$ models the noise in the sensor resistor.

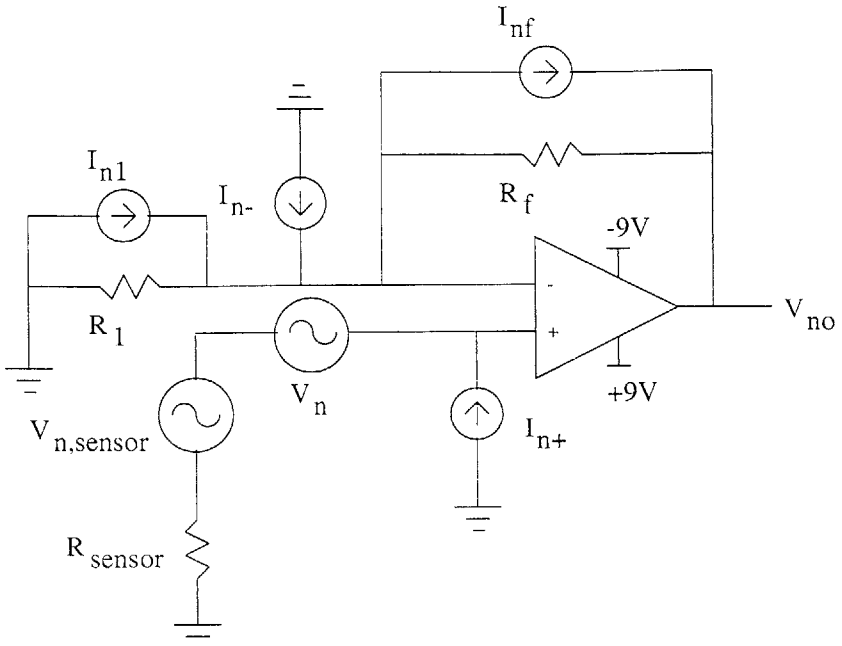

Figure 6.6. Noise Model for Amplifier Circuit with Sensor.

Superposition is once again used to compute the mean-squared noise voltage at the output of this circuit. The mean-squared voltage noise at the output due to current sources $I_{n1}(f)$, $I_{n-}(f)$, $I_{n+}(f)$ is identical to the result shown in (4).

$$V_{no,1}^2(f) = V_{no,amp,1}^2(f) = [I_{n1}^2(f) + I_{nf}^2(f) + I_{n-}^2(f)] \cdot R_f^2 \tag{7}$$

Next, we consider the noise sources at the non-inverting op-amp input. The resulting mean-squared noise voltage at the output is shown in (8).

$$V_{no,2}^2(f) = [V_n^2(f) + I_{n+}^2(f) R_{sensor}^2 + V_{n,sensor}^2] \cdot [1 + \frac{R_f}{R_1}]^2 \tag{8}$$

The total mean-squared noise voltage at the output is given in (9).

$$V_{no}^2(f) = V_{no,1}^2(f) + V_{no,2}^2(f) \tag{9}$$

Subtracting (6) from (9) indicates the excess noise introduced by the sensor resistor. As shown in (10), the excess noise is due to the sensor noise and the op-amp's input current noise.

$$V_{no,excess}^2(f) = V_{no}^2(f) - V_{no,amp}^2(f) = [I_{n+}^2(f)R_{sensor}^2 + V_{n,sensor}^2] \cdot [1 + \frac{R_f}{R_1}]^2 \qquad (10)$$

Finally, the mean-squared voltage noise generated across the sensor is deduced as shown in (11). The input current noise of the op-amp will not be verified experimentally. We will assume that the input current noise is white noise. Furthermore, we will assume that its magnitude is consistent with the values specified in the amplifier datasheet and small compared to other noise sources.

$$V_{n,sensor}^2(f) = \frac{V_{no,excess}^2(f)}{(1 + \frac{R_f}{R_1})^2} - I_{n+}^2 R_{sensor}^2 = 4k_b TR + \frac{k_m I^2}{f^\alpha} \qquad (11)$$

Several factors must be considered when designing the amplifier circuit. The noise of the op-amp and the sensor are assumed to be uncorrelated. Hence, the noise contributions of the op-amp and the sensor are added in a root sum square fashion. The voltage noise of the op-amp and sensor are both referred to the positive input of the op-amp. Hence, both noise sources are amplified by $1 + \frac{R_F}{R_1}$. Therefore, it is important to choose an op-amp that can be configured such that the sensor noise dominates over the amplifier noise. The op-amp used in this circuit is the Analog Devices AD797 ultralow noise op-amp. At frequencies above 1kHz, the input-referred voltage noise of the op-amp is $0.9\frac{nV}{\sqrt{Hz}}$ [21]. The AD797 has a lower white noise density when compared to other commonly used low-noise op-amps, such as the OP27, which has an input-referred voltage noise density of $3\frac{nV}{\sqrt{Hz}}$. The AD797 has a 50nV peak-to-peak input voltage noise in the 0.1Hz to 10Hz frequency range, whereas the OP27 has an 80nV peak-to-peak input voltage noise in the same range [21]. The anticipated Johnson noise in the sensor

resistor is approximately 4.5 $\frac{nV}{\sqrt{Hz}}$ while the anticipated flicker noise for a typical metal-film resistor is between 0.02μV and 0.2μV in the 0.1 Hz to 10Hz frequency range [19]. The noise specifications quoted in the AD797 datasheet suggest that the sensor noise can be deduced reliably using the experimental design described. The one limitation of the AD797 is its high 1/f noise corner. The 100Hz 1/f corner of the AD797 may interfere with our ability to determine the 1/f corner of the sensor noise if it falls below 100Hz [21].

Several factors must also be considered when choosing resistors R_1 and R_f. Gain resistors R_1 and R_f are chosen such that their electrical resistances and composition minimize their noise contribution at the output of the amplifier. A 10Ω resistor is used for R_1 and a 10kΩ resistor is used for R_f. Resistors fabricated from different materials have different flicker noise characteristics as shown in Table 6.1. Table 6.1 suggests that the gain resistors should be wire wound. However, wire wound resistors are uncommon in current practice. Metal film resistors were used instead because they have a comparable noise performance and are readily available. R_1 and R_f are selected from the RN55 variety of nickel chrome metal film resistors.

Table 6.1. Excess noise in RMS microvolts per volt applied across resistor for different resistor types. From [19].

Resistor Type	Excess Noise
Carbon composition	0.10μV to 3.0μV
Carbon film	0.05μV to 0.3μV
Metal film	0.02μV to 0.2μV
Wire wound	0.01μV to 0.2μV

Additionally, the measurement set-up is designed to minimize 60Hz interference. The circuits are placed in a well-shielded box and powered from 9 volt batteries.

6.3 Experimental Results

In the first experiment, the noise characteristic of the op-amp circuit is measured in the absence of the sensor resistor. The noise at the output of the circuit is measured using the HP35670A dynamic signal analyzer over a frequency range from 1Hz to 10kHz. The analyzer was programmed to average the output noise voltage density over 100 trials to improve the accuracy of the readings. Spot noise measurements were then taken at different frequencies in the 1Hz to 10kHz range. The results are shown in Figure 6.7. The mean-squared output voltage noise can be approximated as shown in (12).

$$V^2_{no,amp,measured} \approx \frac{(2.4\mu V)^2}{f^{1.2}} + (960\frac{nV}{\sqrt{Hz}})^2 \qquad (12)$$

The measured results are consistent with the AD797 datasheet and the noise analysis in Equations (4), (5), and (6). The anticipated white noise component of the output noise voltage density was $990\frac{nV}{\sqrt{Hz}}$. The measured value is approximately $960\frac{nV}{\sqrt{Hz}}$, as shown in (12). The white noise of the amplifier dominates at frequencies above 80Hz, which is fairly consistent with the 100Hz 1/f corner shown in the datasheet.

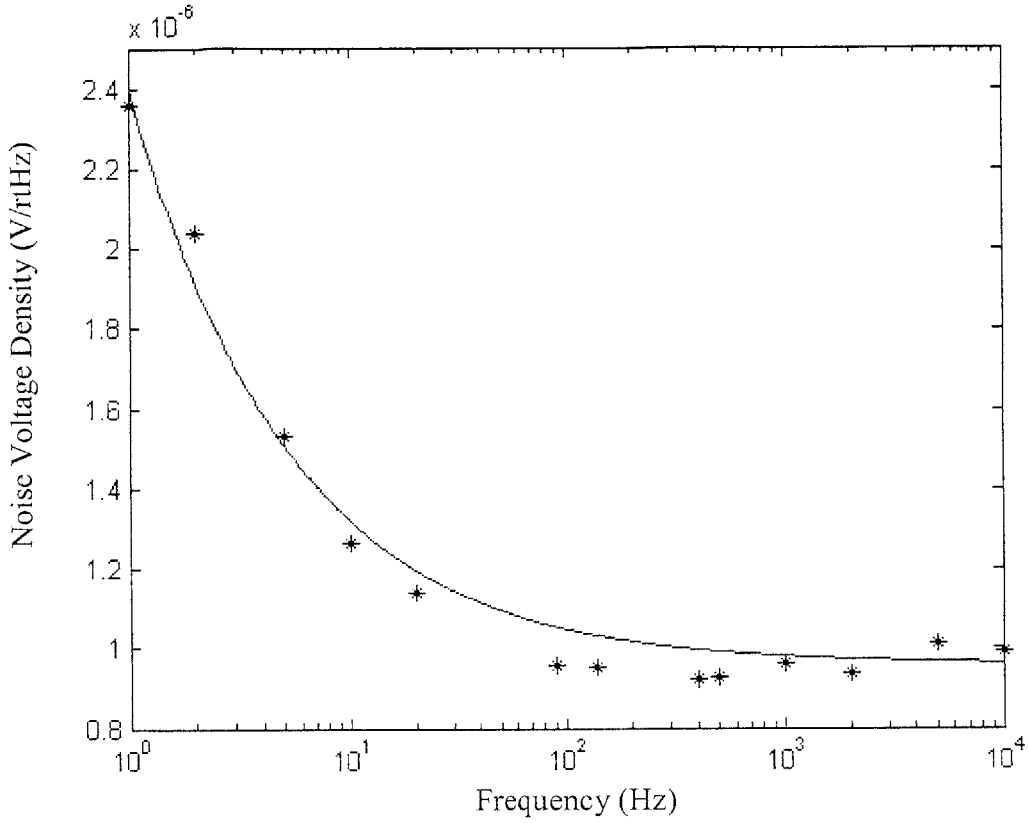

Figure 6.7. Root Spectral Density of Noise Voltage Measured at the Output of the Amplifier Circuit Shown in Figure 6.4. Asterisks represent spot noise measurements taken with the signal analyzer. The smooth curve is fit to the measured data points.

Low frequency noise is measured with an oscilloscope, rather than a spectrum analyzer. The output of the AD797 amplifier is amplified with a differential amplifier and measured with an oscilloscope to capture the noise voltage in the 0.1Hz to 10Hz range. The measured peak to peak input referred noise in the 0.1Hz to 10Hz range was 26nV. The value quoted in the AD797 datasheet is 50nV peak to peak [21]. We assume that the datasheet quotes a worst-case value. Dividing the peak to peak noise voltage by 5.5 yields the RMS noise voltage [22]. The RMS noise voltage in this 01Hz to 10Hz frequency range is 4.7nV.

In the second experiment, the sensor is placed in the op-amp circuit and the noise is measured with the HP35670A signal analyzer as described for the previous

experiment. The results are shown in Figure 6.8. The measured spectral density is approximated by (13).

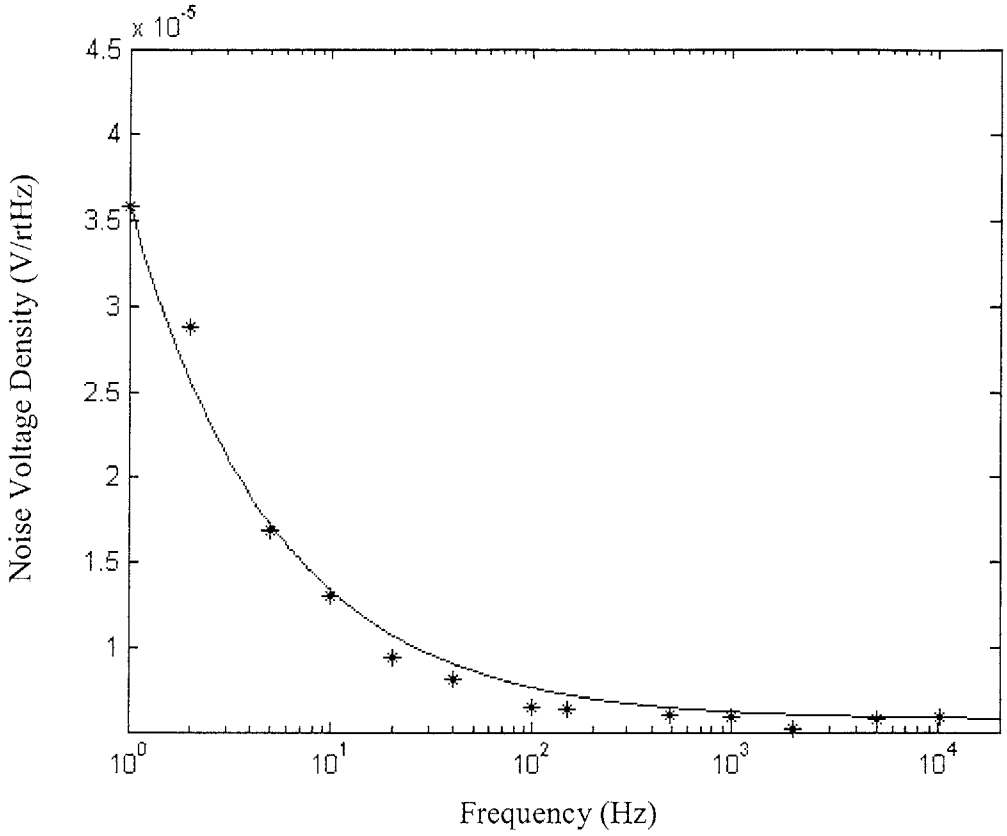

Figure 6.8. Root Spectral Density of Noise Voltage Measured from the Output of the AD797 with the Sensor Resistor Placed Between the Non-Inverting Input and Ground. Asterisks represent spot noise measurements taken with the signal analyzer. The smooth curve is fit to the measured data points.

$$V_{no,measured}^2(f) \approx \frac{(35\mu V)^2}{f^{1.2}} + (5.72\frac{\mu V}{\sqrt{Hz}})^2 \qquad (13)$$

In the 0.1Hz to 10Hz range, the noise is measured with an oscilloscope as described for the previous experiment. The peak to peak input referred noise is 64nV. This corresponds to an RMS noise voltage of 11.6nV.

Finally, the results of the two experiments are combined to determine the noise spectral density of the sensor resistor alone. Using (11) and the $2\frac{pA}{\sqrt{Hz}}$ input current

noise specification from the AD797 datasheet we find the express the power spectral density of sensor resistor noise in (14).

$$V_{n,sensor}^2(f) = \frac{(35nV)^2}{f^{1.2}} + \left(5.0\frac{nV}{\sqrt{Hz}}\right)^2 \tag{14}$$

The measured Johnson noise is approximately $5.0\frac{nV}{\sqrt{Hz}}$. This figure is within 10% of the theoretical value computed using (1). The root spectral density of the sensor is shown in Figure 6.9. From Figure 6.9, we see that the Johnson noise of the sensor clearly dominates at frequencies above 100Hz.

The DC current through the sensor resistor when placed in the amplifier circuit was measured to be 0.16μA. Using (11) and (14) we can express the power spectral density as shown in (15).

$$V_{n,sensor}^2(f) = \frac{0.05\Omega^2 \cdot I^2}{f^{1.2}} + \left(5.0\frac{nV}{\sqrt{Hz}}\right)^2 \tag{15}$$

At this DC current level, the peak to peak noise voltage of the sensor in the 0.1Hz to 10Hz range is 58nV.

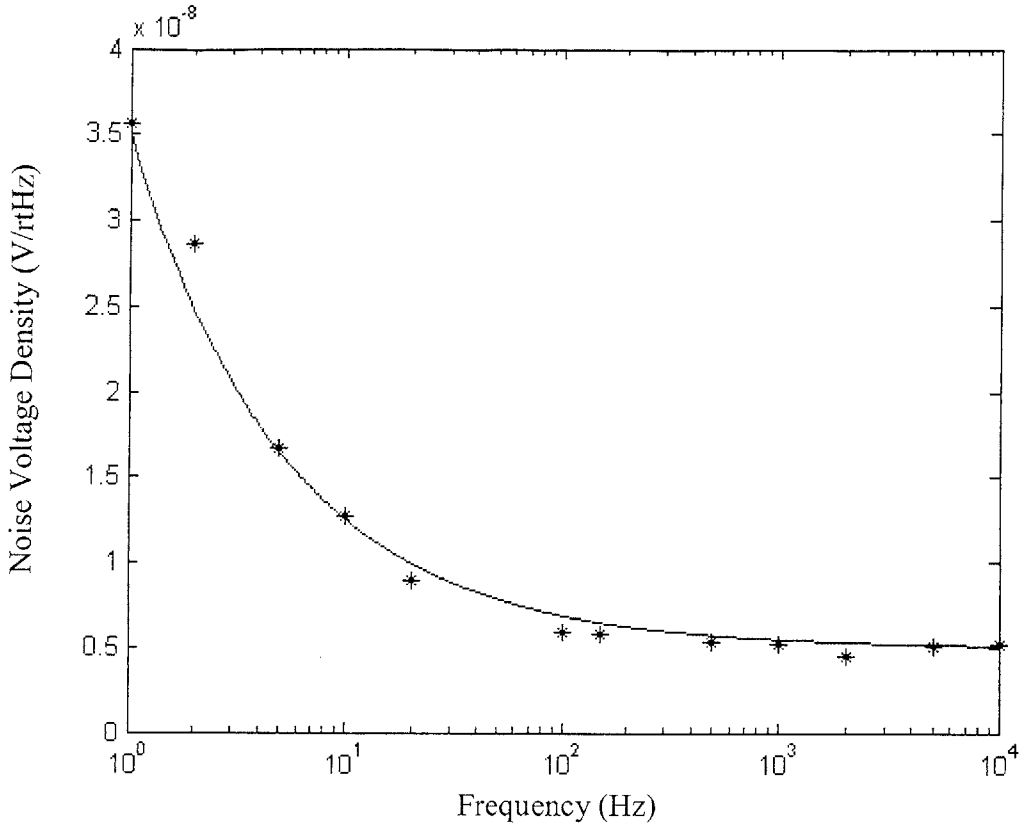

Figure 6.9. Experimentally Derived Root Spectral Density of Sensor Resistor Noise. The asterisks represent points calculated from raw data. The smooth line is a curve fit to the data.

6.4 Minimum Detectable Heat

The results from the noise characterization can be used to determine a best-case estimate of the calorimeter's ability to resolve energy changes. We assume that the flicker noise varies with the square of the DC current and that the DC current through the sensor is 250 μA. The voltage noise density is then expressed as shown in (16).

$$V_{n,sensor}(f, I = 250\mu A) \approx \frac{5.6e-5}{f^{0.6}} + 5.0e-9\left[\frac{V}{\sqrt{Hz}}\right] \tag{16}$$

From Chapter 4, we see that when the sensor is biased with a constant DC current, I, changes in the voltage measured across the sensor map to changes in the temperature of the sensor as shown in (17) and (18).

$$V_{sensor} = IR_0(1+\alpha\Delta T) \tag{17}$$

$$\Delta T = \frac{V_{sensor} - IR_0}{IR_0\alpha} \tag{18}$$

For a typical sensor, R_0 is 1200 Ω and α is 0.0021K. Assuming that no heat is transferred to the ambient surroundings, the amount of heat, Q, that caused the temperature change, ΔT is given by (19).

$$Q = C_t\Delta T \tag{19}$$

Equations (17), (18), (19) can be used to derive the power spectral density of the energy change caused by the sensor's resistance fluctuations.

$$Q_{n,sensor}(f,I) = C_t \cdot \frac{V_{n,sensor}(f,I) - IR_0}{IR_0\alpha} \tag{20}$$

$$Q_{n,sensor}(f, I = 250\mu A) \approx \frac{2.6e-6}{f^{0.6}} - 0.014\left[\frac{J}{\sqrt{Hz}}\right] \tag{21}$$

The signal, or energy change caused by a reaction, can be detected when the signal power is greater than the sensor noise power. Integrating (21) over the bandwidth of interest yields a best-case estimate of the minimum detectable energy change that can be sensed by the calorimeter.

6.5 Conclusions and Future Work

As seen from the analytical and measured noise models, the Johnson noise places a lower bound on the sensor noise. It would be ideal to operate over a bandwidth in which the Johnson noise is the dominant noise mechanism. The electronics described in Chapter 4 use a DC current to measure the resistance of the sensor. The signal at the output of the circuit is effectively the product of the current and the resistance. Following

[23], we note that fluctuations in the sensor resistance caused by flicker noise and fluctuations in the sensor resistance caused by temperature changes are both part of the baseband signal. We, therefore, cannot filter the signal to eliminate the effects of flicker noise.

Consequently, understanding the flicker noise of the sensor becomes important. Further experimentation is required to more accurately determine the relationships between sensor noise and resistance, DC current, and temperature. Sensors with significantly different electrical resistances should be characterized to determine the relationship between flicker noise and the nominal electrical resistance of the sensor at room temperature. A biasing circuit can be used to vary the DC current through the resistor to determine its effect on the 1/f noise corner. Increasing the current through the sensor will cause the sensor resistance to increase for two reasons. The sensor resistance will increase because of the increase in flicker noise. The electrical resistance of the sensor will also increase because of self-heating. These two effects must be isolated. The temperature of sensor can be cycled in a programmable oven and variations in the noise can be characterized at various temperatures. The results of such characterization studies can be used to determine whether it is optimal to increase the current through or the electrical resistance of the sensor to increase the signal to noise ratio of the temperature readout circuit.

Chapter 7:

Conclusion

This chapter summarizes the thesis by briefly reviewing the models developed and the experimental measurements performed. Key conclusions derived from the experimental measurements will be reiterated. Suggestions for additional work that may further enhance the characterization of the hotplate will be discussed.

7.1 Summary

This thesis characterized Draper Laboratory's first generation of microcalorimeter hotplates. Chapter 1 provided the motivation for developing a MEMS calorimeter. Chapter 2 elaborated upon the design and fabrication of the Draper's device. Chapter 3 showed the derivation of the time constant for the plate to thermally equilibrate with a reaction. Chapter 3 also presented a lumped-element thermal circuit model to determine the time constant for the plate to equilibrate with the environment. Chapter 4 illustrated a readout circuit used to measure temperature changes in the plate. Chapter 5 presented experimental measurements that were used to validate the analytical thermal model parameters derived in Chapter 3. Chapter 6 characterized the power spectral density of the temperature sensor noise.

7.2 Conclusions

To create a quasi-adiabiatic system, τ_{Rx}, the time constant for the reaction must be much faster than τ_e, the time constant for the plate to equilibrate with the environment. Calculations from the analytical thermal model suggest that τ_e must be increased. In ambient conditions, the heat transfer is dominated by air conduction as shown by both the theoretical and experimental results. The measured results were, however, 30% lower than the calculated results. The air conduction resistance was underestimated in the analytical model. Air conduction from the sides of the plate and from the tethers was neglected. The analytical model shows that τ_e can be increased by operating in an inert purge gas such as Argon because it has a lower thermal conductivity than air. The thermal conductivity of air can be varied in vacuum as shown in Chapter 5. As predicted, decreasing the thermal conductivity of air by operating in vacuum increases τ_e. At the lowest pressure attainable with the vacuum system used in the measurement, the dominant heat transfer mechanism was radiation. The measured radiation resistance and the theoretical radiation resistance were drastically different. This difference was attributed to an overestimate of polyimide's emissivity in the analytical model. The experimental results show that the emissivity of polyimide is 0.48. We conclude that τ_e can be increased by decreasing the area of the plate and constructing the plate with a material of lower emissivity.

The power spectral density of the sensor noise was measured. The Johnson noise of the sensor fell below the noise floor of the spectrum analyzer. Therefore, an amplifier circuit was created to amplify the sensor noise. The amplifier circuit was characterized separately, indirectly leading to the noise characterization of a low noise, low distortion

op-amp. The noise measurements on the sensor show that the sensor has both flicker noise and Johnson noise components. The Johnson noise could be measured to within 10% of the theoretical value. Changes in resistance caused by flicker noise and by temperature changes cannot be distinguished when reading the resistance of the sensor. When a DC current passes through the resistor, resistance changes caused by both mechanisms will appear in the baseband voltage signal generated across the resistor. Hence, the signal cannot be modulated and filtered to limit the flicker noise of the sensor.

7.3 Future Work

Reaction-dependent time constants should be investigated in more detail to better place the time constants that are dependent on the physical design of the calorimeter hotplate.

The development of a finite element model would enhance the analytical thermal model derived in Chapter 3. This model could be used to capture the heating of the plate, conduction through the tethers, conduction through the air, and radiation effects. In addition, it could be used to determine the effect of dispensing a sample on the calorimeter plate.

Further experimentation is required to more accurately determine the relationships between sensor noise and resistance, DC current, and temperature. The results of such characterization studies can be used to determine whether it is optimal to increase the current through or the electrical resistance of the sensor to increase the signal to noise ratio of the temperature readout circuit.

References

[1] Dube, Christopher E., Marc S. Weinberg, Edwin T. Carlen, Mark J. Mescher, Amy Duwel, Keith B. Baldwin, James L. Sitomer. "MEMS Arrays for Label-Free Sensing of Biomelcules." Proceedings of the 5th International Symposium on MEMS and Nanotechnology (5th ISMAN), (Costa Mesa, CA), pp. 541-554, June 7 – 10, 2004.

[2] Hohne, G.W.H, W. Hemminger, and H.-J. Flammersheim. *Differential Scanning Calorimetry: An Introduction for Practitioners*. Berlin: Springer, 1996.

[3] MicroCal. "The Use of Isothermal Titration Calorimetry in Antibody Control and Characterization." 2003. 30 June 2004. <http://www.microcalorimetry.com/index.php?id=58>.

[4] Sundquist, Wes. "Lecture 6: Isothermal Titration Calorimetry." 30 June 2004. <http://www.biochem.utah.edu/wes/teachfiles/Lecture6/Lecture_6_Notes.pdf>.

[5] MicroCal. "What is DSC?" 2003. 28 Nov. 2003. <http://www.microcalorimetry.com/index.php?id=16>.

[6] MicroCal. "What is ITC?" 2003. 28 Nov. 2003. <http://www.microcalorimetry.com/?id=13>.

[7] Gimzewski, J.K., Ch. Gerber, E. Meyer, and R.R. Schlittler. "Observation of a Chemical Reaction Using a Micromechanical Sensor." *Chemical Physics Letters*. 217 (1994): 589-594.

[8] Barnes, J.R., R.J. Stephenson, M.E. Welland, Ch. Gerber, C., and J.K. Gimzewski. "Photothermal Spectroscopy with Femtojoule Sensitivity Using a Micromechanical Device." *Nature*. 372 (1994): 79-81.

[9] Lai, S.L., G. Ramanath, and L.H. Allen. "Heat Capacity Measurements of Sn Nanostructures Using Thin-Film Differential Scanning Calorimeter with 0.2nJ Sensitivity." *Appl. Phys. Lett.* 70 (1997): 43-45.

[10] Woodward, Stephen W. "Efficient Algorithms Improve the Linearization of Platinum RTDs." Electronic Design. 2 Oct 2000. 30 June 2004. <http://www.elecdesign.com/Articles/ArticleID/4793/4793>.

[11] Edwards, C. Henry, and David E. Penney. *Elementary Differential Equations With Boundary Value Problems*. Upper Saddle River: Prentice Hall, Inc., 2000.

[12] Mills, A.F. *Basic Heat and Mass Transfer*. Upper Saddle River: Prentice Hall, Inc.,1999.

[13] General Electric. "Symmetric Temperature Distribution Beyond a Small Disk-Shaped Source." *Heat Transfer Data Book*. New York: Genium Publishing Co.,1984.

[14] Roters, Herbert C. *Electromagnetic Devices*. New York: John Wiley & Sons, Inc., 1970.

[15] Kreith, Frank. *Principles of Heat Transfer*. New York: Intext Press, Inc., 1973.

[16] General Electric. "Thermal Conductivity of Air at Reduced Pressure Between Infinite Parallel Flat Plates." *Heat Transfer Data Book*. New York: Genium Publishing Co.,1984.

[17] McAdams, William H. *Heat Transmission*. New York: McGraw-Hill, 1954.

[18] Keiji, Takagi, Toru Mizunami, and Satoshi Masuda. "1/f Noise Measurement in Semicontinuous Metal Films." *IEEE Transactions on Components, Hybrids, and Manufacturing Technology*, Vol. CHMT-12, No. 4 (1987): 687-689.

[19] Horowitz, Paul and Winfield Hill. *The Art of Electronics*. New York: Cambridge University Press, 1995.

[20] Johns, David and Ken Martin. *Analog Integrated Circuit Design*. New York: John Wiley and Sons, Inc. 1997.

[21] Analog Devices. "Ultralow Distortion, Ultralow Noise Op Amp, AD797*." Oct 2002. 30 June 2004. <http://www.analog.com/UploadedFiles/Data_Sheets/507345751AD797_d.pdf>

[22] Smith, Lewis and D.H. Sheingold. "Noise and Operational Amplifier Circuits." *Analog Dialogue*. Mar 1969: 19-31.

[23] Senturia, Stephen D. *Microsystem Design*. Boston: Kluwer, 2001.